https://doi.org/10.5194/essd-2026-146
Preprint. Discussion started: 12 March 2026

Open Access Earth System Science Data Discussions

Vertical observations of aerosol properties in the Arctic, Antarctic and Alpine atmospheric boundary layers with a tethered balloon

Julia Schmale[1], Roman Pohorsky[1], Yolanda Temel[1], Michael Lonardi[1], Joanna Alden[1,*], Radiance Calmer[1], Evan Thomas[2], Andrea Baccarini[1,+], Nora Bergner[1], Berkay Dönmez[1], Lionel Favre[1], Henrik Helmig[1], Benjamin Heutte[1], Marie Lou Hirschy[1], Romain Phan[1], Orpheas Solidakis[1], Aleksandrina Streltsova[1], Mihnea Surdu[1], Arthur Tabary[1]

[1]Extreme Environments Research Laboratory, École Polytechnique fédérale de Lausanne, Sion, 1951, Switzerland
[2] École Polytechnique fédérale de Lausanne, EPFL Valais Wallis, Sion, 1951, Switzerland
* now at Centre Alpin de Recherche sur les Réseaux Trophiques et Écosystèmes Limniques, Université Savoie Mont Blanc: Chambéry, Auvergne-Rhône-Alpes, FR
+ now at Aerospec, Lausanne, Switzerland

Correspondence to: Julia Schmale (Julia.schmale@epfl.ch)

Abstract.

Information on vertical profiles of aerosols in the lowermost kilometer of the atmosphere is still scarce in general, and particularly in polar regions and complex terrain due to observational limitations. However, the vertical distribution of various aerosol properties, such as the particle number size distributions, are essential climate variables, because aerosols influence Earth's radiation budget and their vertical position in the atmosphere matters. Specifically for aerosol-cloud interactions, the presence and properties of particles able to act as cloud condensation nuclei and ice nucleating particles at cloud level, is critical information. With this data descriptor we aim to start filling the observational gaps systematically, and introduce datasets of vertical aerosol properties from nearly 300 tethered balloon flights between 2022 and 2025 in the Arctic, Antarctica and alpine terrain in Europe. Flights up to 900 m above ground describe various boundary layer conditions throughout all seasons. We describe the processing from raw to level 2 data, provide processing and quick look codes, and give examples of how data may be used and analyzed by the community. All data and code are openly accessible.

1 Introduction

Aerosol-radiation interactions (ARI) and aerosol-cloud interactions (ACI) continue to add uncertainty to anthropogenic radiative forcing, and specifically ACI is the largest single contributor to the overall uncertainty (e.g., Bellouin et al., 2020; Gordon et al., 2023). In part this challenge is due to a lack of observations of the vertical distribution of aerosols and their properties. For example, the efficacy of the climatic effect of black carbon at the surface depends strongly on the height above ground, where the absorbing particles reside, and in which geographical region (Flanner, 2013; Samset et al., 2013). In the Arctic, black carbon has the strongest effect in the lowermost part of the atmosphere, while presence at high altitudes is much less effective (Flanner, 2013). With reference to ACI, the number and size of aerosol particles at the height, where clouds form

https://doi.org/10.5194/essd-2026-146
Preprint. Discussion started: 12 March 2026

and act as cloud condensation nuclei (CCN) and ice nucleating particles (INP), will influence the cloud droplet number concentrations and size distributions as well as the presence of ice crystals (Carslaw et al., 2013; Kanji et al., 2017). The resulting cloud microphysics determine cloud radiative properties (e.g., Zelinka et al., 2014) and precipitation processes (e.g., Rosenfeld et al., 2014).

To capture the potential effects of ARI and ACI, surface-based observations alone are not sufficient, because aerosol concentrations and properties near the ground are not necessarily representative of those aloft due to the structure of the troposphere, and vertical transport and atmospheric chemical processes (Clarke and Kapustin, 2010). Aerosol properties in the free troposphere are typically different from the boundary layer (e.g., Brock et al., 2019; Collaud Coen et al., 2011; Engelmann et al., 2021), and even within the remote and urban boundary layer (BL) they might vary substantially (Lei et al., 2021; Pilz et al., 2024; Pohorsky et al., 2025b; Rosati et al., 2015). This variation owes to the thermodynamic structure, particularly inversions that can occur at the surface (surface-based inversion) or at elevated heights (elevated inversions) within the BL (Ferrero et al., 2016; Pace et al., 2015; Prasad et al., 2022; Thomas et al., 2019). Those typically inhibit the up-mixing of surface emissions and the down-mixing of elevated aerosol sources.

Observations aiming to elucidate the climatic effects of ARI and ACI are however often confined to the surface, e.g., in established monitoring networks such as Global Atmosphere Watch (GAW) or the European Aerosols, Clouds and Trace Gases research infrastructure ACTRIS (e.g., Asmi et al., 2013), because regular vertical profiling for in situ measurements is challenging. The challenge results e.g., from the weight and complexity of the instruments such that operation typically requires research aircraft with operators or helicopters towing complex flying laboratories (Pätzold et al., 2023; Siebert et al., 2021). This means that both ARI and ACI processes as well as essential climate variables (ECVs) of aerosols and clouds are not easy to observe along vertical profiles. Vertical ECVs of aerosols include, amongst others, particle number size distribution, number of CCN, and optical properties such as extinction coefficients and single scattering albedo (The 2022 GCOS Implementation Plan (GCOS-244), 2025). ECVs of clouds are, amongst others, cloud droplet effective radius and cloud liquid and ice water contents. In addition to ECVs, detailed process observations are necessary to gain insights into unresolved questions, for example: in which thermodynamic conditions are surface-based observations representative of aerosol properties at cloud level; whether clouds are seeded by aerosols from below, aloft or both in varying thermodynamic conditions; or whether the number of INP can explain the number of ice crystals or if secondary ice processes are at work.

Remote sensing, and specifically ground-based remote sensing, can deliver information on cloud properties and to a certain degree also on aerosol properties along the vertical profile (Ansmann et al., 2023; Engelmann et al., 2021; Radenz et al., 2024). However, unless the suite of remote sensing instrumentation is highly sophisticated, uncertainties can remain large and certain proxies, e.g., for aerosol and cloud droplet number size distributions, cannot be retrieved (Gast et al., 2025; Schlosser et al., 2022). In recent years, there have been significant advances in vertical observations of the aerosol and cloud ECVs mentioned above, mainly through development and deployment of uncrewed aerial vehicles (Altstädter et al., 2015; de Boer et al., 2022;

https://doi.org/10.5194/essd-2026-146
Preprint. Discussion started: 12 March 2026

Lappin et al., 2024; Pätzold et al., 2023) and tethered balloons (Creamean et al., 2021; Ferrero et al., 2016; Pasquier et al., 2020; Pilz et al., 2022; Pohorsky et al., 2024; Porter et al., 2020), as well as due to progress in miniaturized high-quality instrumentation (Liu et al., 2021b; Pilz et al., 2022; Pohorsky et al., 2024). Nevertheless, in situ vertical measurements of aerosols and clouds remain sparse. Consequently, there remains a gap in information on ECVs, other variables and in process understanding (Creamean et al., 2021; Pilz et al., 2024; Schmale et al., 2021). Filling this gap is important to constrain satellite-based observations that have a larger temporal and geographical coverage than in situ measurements, as well as numerical simulations that ultimately determine the climatic effects of ARI and ACI.

Here, we present quality assessed data on aerosol and cloud droplet properties from tethered balloon (Helikite, Allsopp, UK) observations in the BLs and lower free troposphere of the Arctic, Antarctica and mountainous terrain in Europe. The overall number of flights is 276 up to an altitude of 990 m above ground at the time of writing this manuscript. We focus on polar and mountain BLs because they often feature multiple layers of aerosols due conditions with reduced vertical mixing (e.g., Jozef et al., 2023; Rotach and Zardi, 2007), and specifically in polar regions, low level clouds within or at the top of the BL exert a strong effect on the surface energy budget (Shupe and Intrieri, 2004). This data descriptor provides information on how data were processed, which uncertainties to expect, and provides guidance on how the data can be used for scientific research.

2 Overview on campaigns

Campaigns were carried out between 2021 and 2025 in nine locations, thereof five in the Arctic, one in coastal Antarctica, two in the Swiss Alps, and one in the Greek Peloponnese mountains (see details in Table 1 and map in Fig. 1). An online overview map (https://www.epfl.ch/labs/eerl/eerl-home-page/research/field-work-overview/) provides interactive information on locations, associated publications and collaboration partners. Here, we briefly present the purpose and larger context for each campaign.

Arctic campaigns: The common denominator for these campaigns is the characterization of aerosol layers throughout the often-stratified Arctic BL and the investigation of in how far surface observations can be representative of aerosol above the surface mixed layer, which can be as shallow as 20 m (Pohorsky et al., 2025b). Specifically, the Alaskan Layered Pollution And Chemistry Analysis (ALPACA) project focused on extreme wintertime urban pollution and BL stratification (Simpson et al., 2024) as well as the up-mixing of surface and down-mixing of power plant emissions (Pohorsky et al., 2025b). Observations at Villum Research Station with the CLeancloud Arctic VIllum ExpeRiment (CLAVIER) focused on the transition period between winter and spring, within a highly stratified BL including haze from long-range transport, new particle formation events, and a warm air-mass intrusion. The GreenFjord campaign aimed to investigate the vertical footprint of climate-relevant aerosol properties of local urban emissions in an environment which is otherwise influenced by marine emissions and occasional long-range transported pollution (Alden et al., 2025b). The Pallas Cloud Experiment (PaCE) was geared towards understanding the vertical extent of new particle formation and aerosol-cloud interactions in a boreal environment (Brus et al.,

https://doi.org/10.5194/essd-2026-146
Preprint. Discussion started: 12 March 2026

2025). And finally, the ARTofMELT (AOM) expedition focused on the melt onset in the marginal ice zone and the role of aerosol-cloud interactions for the surface energy budget.

Antarctic campaign: The project 'ORigin of Antarctic CLoud particles and their Effects on the Surface radiation budget' (ORACLES) investigates the vertical profiles of aerosol properties and ACI as a function of marine and Antarctic continental air masses as well as the BL structure at Neumayer III Station operated by the Alfred Wegener Institute.

Alpine campaigns: Both Brigerbad and Turtmann are located in the narrow Rhone valley of the Swiss Alps, where dynamic air mass movement is induced by down and up-valley winds in the morning and afternoon, respectively, as well as by the appearance of sunlight on the slopes and valley floor. Focus was on the dispersion of aerosols during transition seasons, i.e., between summer and winter in Brigerbad, and winter to summer in Turtmann. In Greece, observations were carried out half-way up Mt. Helmos with the Cleancloud Helmos OrograPhic sIte experimeNt (CHOPIN) with the aim to measure aerosol properties throughout the evolution of the mountain BL and aerosol-cloud interactions under local and long-range transported aerosol pollution.

Table 1: Overview information on flights per campaign. SBI means surface-based inversion, EI means elevated inversion.

Campaign	Environment	Dates	Coordinates, elevation above ground level (a.s.l.)	Helikite model	No. of flights	Maximum flight altitude	No. of cloud cases	No. of inversions
ALPACA	Suburb of Fairbanks, Alaska, USA	2022-01-26 to 2022-02-25	64.853 N, 147.859 W, 138 m	45 m^3	24	345 m	0	14 (SBI) 4 (EI)
ARTofMELT	Arctic Ocean, marginal ice zone	2023-05-16 to 2023-06-10	80.482 to 78.842 N, 3.778 W to 6.267 E, 0 m	45 m^3	23	645 m	10	4 (SBI) 10 (EI)
Brigerbad	Narrow alpine valley surrounded by high mountains	2021-09-22 to 2021-10-14	46.300 N, 7.921 E, 652 m	45 m^3	26	760 m	0	9 (SBI) 0 (EI)
CHOPIN	Peloponnese (Greece), mountain ski resort	2024-10-23 to 2024-11-05	38.005 N, 22.198 E, 1700 m	45 m^3	23	527 m	8	2 (SBI) 8 (EI)
CLAVIER	Northern	2024-03-	81.581 N,	45 m^3	57	750 m	2	48 (SBI)

https://doi.org/10.5194/essd-2026-146
Preprint. Discussion started: 12 March 2026

Open Access Earth System Science Data Discussions

	Greenland, flat terrain near coast	23 to 2024-05-02	16.641 E 30 m				(fog)	4 (EI)
GreenFjord	Southern Greenlandic fjord system	2023-06-27 to 2023-08-02	60.916 N, 46.053 W, 17 m	64 m^3	24	780 m	7	7 (SBI), 14 (EI)
ORACLES	Coastal Antarctic, flat terrain, 6 km from coast	2024-12-22 to 2025-02-15	70.662 S, 8.286 W 40 m	24 m^3 and 64 m^3	68	992 m	21	11 (SBI) 23 (EI)
PaCE	Boreal forest	2022-09-28 to 2022-10-13	68.000 N, 24.239 E 334 m	45 m^3	19	539 m	12	1 (SBI), 10 (EI)
Turtmann	Narrow alpine valley surrounded by high mountains	2024-02-07 to 2024-02-28	46.305 N, 7.691 E, 640 m	64 m^3	12	700 m	0	5 (SBI) 4 (EI)

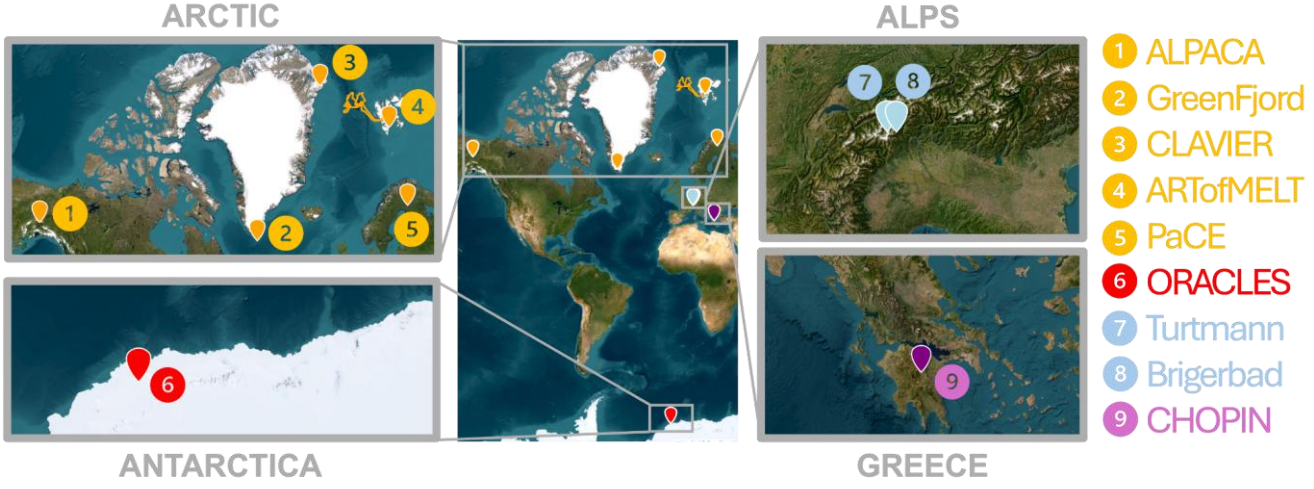

Figure 1: Map of campaign locations. Basemap tiles: Esri | Powered by Esri, DigitalGlobe, GeoEye, i-cubed, USDA FSA, USGS, AEX, Getmapping, Aerogrid, IGN, IGP, swisstopo, and the GIS User Community.

https://doi.org/10.5194/essd-2026-146
Preprint. Discussion started: 12 March 2026

Open Access Earth System Science Data Discussions

3 Instrumentation

The EERL Helikite payload is called MoMuCAMS (Fig. 2) for 'Modular Multiplatform Compatible Atmospheric Measurement System'. The instruments have previously been described and characterized in Pohorsky et al. (2024 and references therein). Since that publication, more instruments have been included for regular operations, specifically, a handheld condensation particle counter (CPC model 3007, TSI), a Partector 2 (Naneos), a microAethalometer (microAeth, Aethlabs), a miniaturized Cloud Droplet Analyzer (miniCDA, Palas) and a light optical aerosols counter (LOAC, LPC2E – CNRS). Table 2 provides a summary of all instruments operated per campaign.

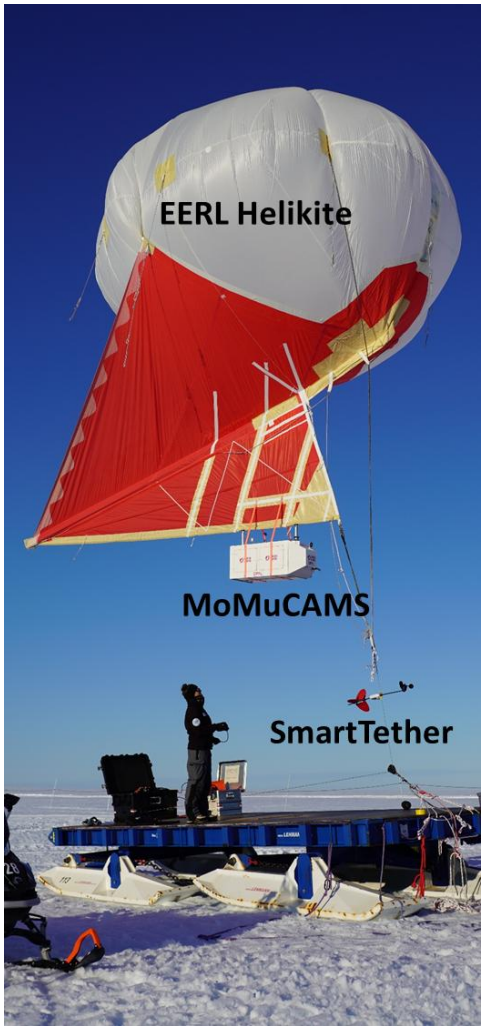

Figure 2: The Extreme Environments Research Laboratory (EERL) Helikite with payload MoMuCAMS and SmartTether during deployment at Neumayer Station III, Antarctica, 2025. Picture credid: M. Lonardi.

https://doi.org/10.5194/essd-2026-146
Preprint. Discussion started: 12 March 2026

Particle counters and particle number size distributions. The aerosol number size distribution is obtained from the miniaturized Scanning Electrical Mobility Sizer (mSEMS model 9404, Brechtel Manufacturing Inc.) and the Portable Optical Particle Spectrometer (POPS, Handix Scientific). The mSEMS measures the electrical mobility diameter of particles ranging from 8 to a maximum of 300 nm. The time resolution depends on the selected size resolution (number of bins) and the time spent measuring in each size bin. These parameters are typically defined according to the local environment and ambient aerosol concentration. For an urban environment, a 60-bin resolution with a 1 s bin time was selected, yielding a 1-min scan time (Pohorsky et al., 2025b). In pristine areas, where concentrations can fall below 10 cm^{-3}, the bin time needs to be increased to allow for sufficient counting statistics (Alden et al., 2025b). To limit the overall scan time, the number of bins is typically reduced (e.g., 40 bins).

The POPS measures the optical diameter of particles ranging from ~150 nm to > 3 µm. The optical diameter is obtained from the scattering signal of particles sampled through a laser beam and converted to a size, assuming a spherical diameter with a refractive index of 1.615+0.001i at 405 nm (i.e., refractive index of polystyrene latex spheres). Note that these assumptions can lead to sizing errors in environments with highly absorbing and/or non-spherical particles. The POPS records data at a 1 Hz resolution and classifies particles into 16 log-spaced size bins. For both instruments, the concentrations in each bin are normalized (i.e., expressed as *dN/dlogDp*) to account for the logarithmic bin spacing.

For the total aerosol number concentration, the advanced Mixing Condensation Particles Counter (aMCPC model 9403, Brechtel Manufacturing Inc.) or the handheld Condensation Particle Counter (CPC3007, TSI) are used. The size detection cut-offs (d_{50}) are approximately 7 and 10 nm, respectively, and data are recorded at a 1 Hz time resolution and expressed in particles per cubic centimeter (cm^{-3}). The handheld CPC is a well characterized concentration particle counter, which has also been used in polar regions (Pilz et al., 2023).

The Partector 2 is a nanoparticle detector (Fierz et al., 2014, 2015) occasionally deployed as a backup particle counter on the MoMuCAMS due to its low weight (415 g) and ease of use. The instrument uses an open-path electrometer followed by an electrostatic deposition stage and another open-path electrometer in an in-series configuration, operating with a flow rate of 0.5 l min^{-1} (Bezantakos et al., 2024). The Partector 2 detects particles in the size range of 10 to 300 nm, covering concentration ranges between 0 and 10^6 particles cm^{-3}. The measurements are obtained with 1 Hz temporal resolution, additionally recording ambient pressure for subsequent altitude calibration. The calibrated data, has a 30% uncertainty in the accuracy (https://www.naneos.ch/partector2.html). Poor signal to noise ratio can be overcome by averaging over time.

Droplet number size distribution. The miniaturized cloud droplet analyzer (miniCDA, Palas Gmbh) is a new, miniaturized optical particle counter for cloud droplets (Solidakis, 2024). It has a specific inlet oriented vertically and protected against precipitation, providing a flow rate of 2.8 l min^{-1}. The measurements can be used to derive ECVs such as droplet effective radius and liquid water content. The instrument detects hydrometeor and particle size distributions in the range of 0.24 to 43 µm using 256 manufacturer-calibrated size bins, covering concentration ranges between 0 and 600 droplets cm^{-3}. The measurements are obtained with a 1.5 s temporal resolution, complemented by pressure measurements (every 15 s), which are

https://doi.org/10.5194/essd-2026-146
Preprint. Discussion started: 12 March 2026

used for data synchronization with the MoMuCAMS flight computer. There are no peer-reviewed publications yet on this instrument.

The LOAC has been used during the ARTofMELT campaign to measure the size distribution of water droplets in (Renard et al., 2016). The LOAC measures the aerosol and droplet size distribution from 0.2 to 50 µm, at a time resolution of 30 s. Two detectors measure the scattering, at 12° and 60°, produced by the sampled particles traveling through a laser beam. The intensity of the forward scattering signal is used to measure the size of the particles and the difference between the two angles provides additional information to classify particles types (e.g., carbonaceous, minerals, liquid droplets).

The miniCDA is deployed with larger balloons, while the LOAC is routinely deployed on balloons smaller than 24 m^3.

Optical properties. For light absorbing particles, filter-based absorption detection instruments are used. The single Channel Tricolor Absorption Photometer (STAP model 9406, Brechtel Manufacturing Inc) provides the aerosol light absorption coefficient at three wavelengths (450, 525 and 624 nm, e.g., Pilz et al., 2022). The absorption data are initially recorded at a 1 Hz resolution and then averaged over a longer integration time. For a 2-min integration, the detection limit of the instrument is 0.2 Mm^{-1}, which corresponds to an equivalent black carbon (eBC) mass concentration of about 20 ng m^{-3} (Bates et al., 2013).

The MicroAeth (MA200, AethLabs) is also a filter-based absorption photometer measuring aerosol light attenuation at five wavelengths (375, 470, 528, 625 and 880 nm, Liu et al., 2021a). Aerosols are continuously deposited onto a Polytetrafluoroethylene (PTFE) filter band, and the attenuation through the filter is then related to an eBC mass concentration. On MoMuCAMS, measurements were recorded at 60 s time resolution in SingleSpot™ mode for a detection limit of 30 ng m^{-3} eBC for a 5-min average at a 150 ml min^{-1} flow rate.

The choice between STAP and MicroAeth depends on instrument weight and expected ambient eBC concentrations.

Particle sampling. An 8-channel filter sampler (FILT Model 9401, Brechtel Manufacturing Inc., USA) enables time-resolved aerosol collection on various filter media. The FILT can operate at a flow rate between 0.5 and 3.3 lpm with an accuracy of ±5%. The sampling channel can be switched remotely, allowing up to 8 samples to be collected during a single flight. Housekeeping data of the FILT, including channel position and flow rate are recorded at a 1 Hz time resolution and used afterwards to calculate the total sampled volume.

Trace gases. CO is measured with the Mira Pico (Aeris Technologies). The Mira Pico is based on non-dispersive infrared (NDIR) spectroscopy. For ground-based operations, the instrument is operated with a CO scrubber, which allows for continuous corrections of the instrument's baseline (zero measurement) and a ppb level accuracy according to the manufacturer. This mode of operation reduces the time resolution. For vertical profiling, the instrument is operated in its "manual" mode (without live baseline corrections). The time resolution is 1 Hz and the uncertainty reaches a maximum of 17 ppb due to potential fluctuations of the baseline during the flight (Pohorsky et al., 2024).

https://doi.org/10.5194/essd-2026-146
Preprint. Discussion started: 12 March 2026

CO_2 is measured with an infrared sensor (GMP343, Vaisala). The instrument measures the absorption of a NDIR beam by CO_2 molecules through an open path cavity. A sensor switches every second between the absorbing band of CO_2 and a reference wavelength, yielding a measurement time resolution of 2 s with an accuracy of 3 ppm +/- 1% according to the manufacturer. O_3 is measured with the Dual Beam Ozone monitor (model 205, 2BTech). The instrument measures the intensity reduction of a UV beam from O_3 molecules. A reference detection cell with an O_3 scrubber is used in parallel to improve its accuracy. The time resolution of the O_3 monitor is 2 s with an accuracy of 1 ppb or 2% of the readings for 10-s averaged data.

Meteorological variables. On the MoMuCAMS payload, meteorological variables are obtained from various sensors placed on the outside of the instrumental platform and complement the information of aerosol and trace gas measurements. Temperature and relative humidity (both with a pair of sensors SHT85, Sensirion), barometric pressure (BME280, Bosch), wind speed and wind direction (LI-550 TriSonica Mini, LiCOR) are typically recorded at a 1 Hz time resolution. In addition, a SmartTether Weather Sonde (ST, Anasphere, Inc.) measures the latitude and longitude, temperature, relative humidity, pressure, as well as wind speed and wind direction. The SmartTether operates at a 1 s time resolution with accuracies of ±0.5 mbar for pressure, ±0.5°C for temperature, ±1.7% for RH, ±0.1 m/s or 5% (whichever is greater) for wind speed, and ±2 degrees for wind direction.

GPS. GPS coordinates and attitude angles (pitch, roll, and yaw angles) are collected during flights with a VN200 GNSS/INS (VectorNav).

https://doi.org/10.5194/essd-2026-146
Preprint. Discussion started: 12 March 2026

Open Access Earth System Science Data Discussions

214

215 **Table 2: Overview of instruments operated on each campaign. An 'x' denotes that the instrument was operated in general, however**
216 **not necessarily on every flight.**

	Thermo-dynamics		particle number concentration and size distribution					Droplet number concentration		Aerosol absorption properties		Samp-ling	Trace gases		
Instrument	T and RH sensor	SmartTether	m-SEMS	a-MCPC	CPC-3007	Partector2	POPS	LOAC	miniCDA	STAP	microAeth	FILT	CO_2	Pico CO	Ozone
ALPACA	x		x				x			x		x	x	x	x
ARTofMELT	x	x	x				x	x		x		x			
Brigerbad		x	x	x			x			x		x	x	x	x
CHOPIN	x	x	x	x			x		x	x	x		x		
CLAVIER	x	x	x				x		x	x		x			
GreenFjord	x	x	x	x			x			x		x	x		x
ORACLES	x	x	x	x	x		x		x			x			
PaCE	x	x	x	x	x	x	x			x		x	x		
Turtmann	x	x	x				x			x			x		

217

218

https://doi.org/10.5194/essd-2026-146
Preprint. Discussion started: 12 March 2026

Open Access Earth System Science Data Discussions

4 Data Processing and example analyses

4.1 Work flow and data levels

The MoMuCAMS is operated with a custom-made flight computer (FC), which collects data from most instruments and provides a reference time stamp and one merged raw data file. Data from instruments, which are not connected to the flight computer, are downloaded separately. To handle the various input files, a 'hElikite dAta proceSsing codE' (EASE) was developed in Python. The code is structured such that future additional instrument files can be integrated. The objective of the processing code is to generate quality controlled and assured data in a standard and traceable way before conducting scientific analyses. It also ensures a homogenization of data processing steps and data products for different measurement campaigns. Figure 3 summarizes the workflow. The following description provides details on the processing of data from raw to the final level 2 with Table 3 providing a summary of all steps. The definition of levels follows in principle the guidelines by EBAS (https://ebas-submit.nilu.no/), the data base of the ACTRIS network.

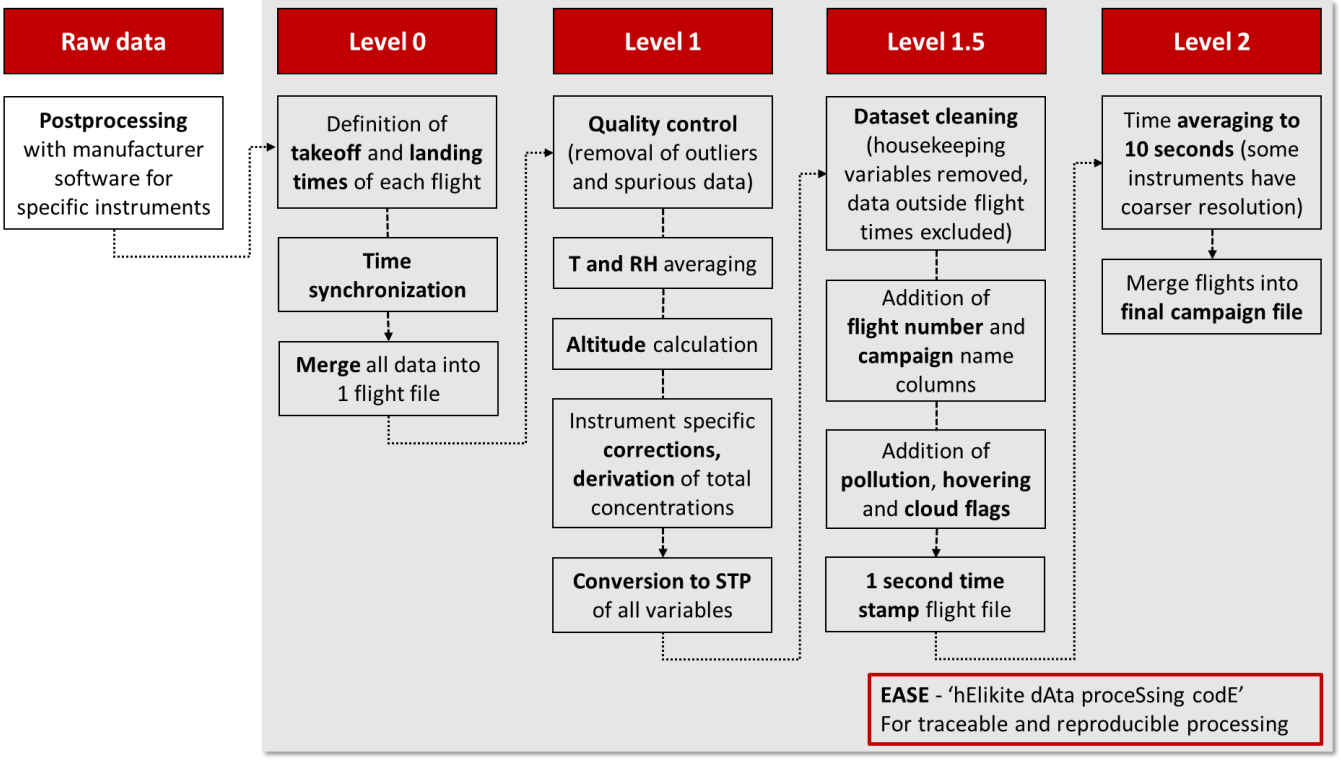

Figure 3: Workflow diagram for EERL helikite data processing with the 'hElikite dAta proceSsing codE' (EASE).

https://doi.org/10.5194/essd-2026-146
Preprint. Discussion started: 12 March 2026

Open Access Earth System Science Data Discussions

4.1.1 Raw data

Files directly generated from individual instruments are considered raw data and are imputed to EASE. There are exceptions for two instruments, the STAP and mSEMS, because they require specific processing to obtain the desired variables. Codes from the manufacturer to be run in Igor Wave Metrics are executed manually first and the output files are subsequently used in EASE. For the STAP, the absorption coefficients are calculated based on a methodology developed by Ogren (2010). For the mSEMS, an inversion routine as described in Wiedensohler et al. (2012), is applied to the raw particle counts to calculate the particle number size distributions from the measured electrical mobility distributions. After these steps, all data are treated to create level 0 (L0).

4.1.2 Level 0 data processing

At the end of the L0 processing step, all instrumental data are time synchronized, the start and end of each flight are defined as takeoff and landing, and all variables are merged into one data file per flight.

While all internal clocks of instruments are synchronized at the beginning of each measurement campaign, time drifts of up to a few seconds can occur. These drifts lead to shifted time series and vertical misalignments between the different variables, which are not directly saved by the central flight computer. Because of the vertical motions of the Helikite, the variations in the high-resolution pressure readings of each instruments allow to identify these time shifts. Using a cross-correlation function for two independent variables, we use the pressure readings of the instruments to identify shifts between each instrument and a reference instrument, whose time is known to be correct (i.e., flight computer). To find the time lag (τ) between instruments' clocks, the pressure time series of the unsynchronized instrument is shifted by 1-s steps within a time window of ± 180 s with reference to the flight computer's time. A Pearson correlation between the two pressure time series is then computed at each τ. The τ with the highest Pearson correlation is then defined as the instrument's time shift and used to time synchronize the measurements of the latter. Figure 4 illustrates the process.

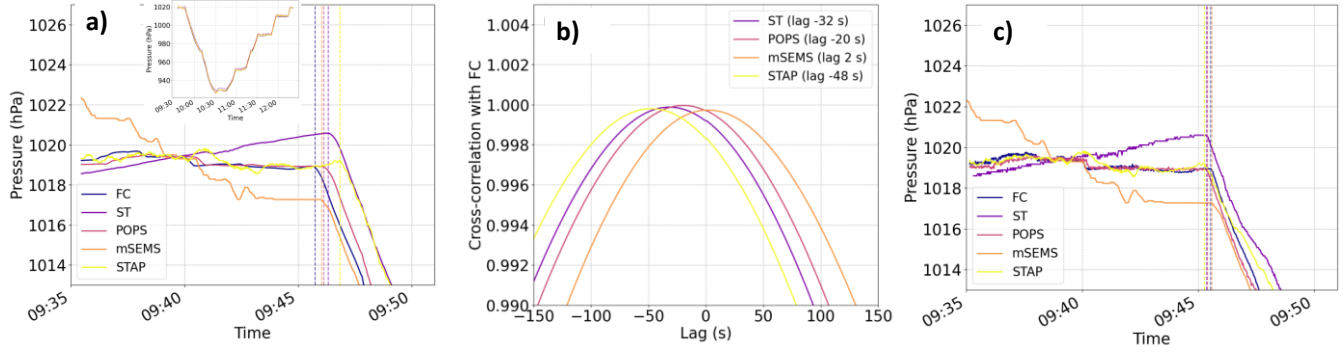

Figure 4: Example of time synchronization based on pressure data. The legend refers to individual instruments, where FC is flight computer, and ST is SmartTether. a) Time series before synchronization, the insert shows pressure time series for the entire flight,

https://doi.org/10.5194/essd-2026-146
Preprint. Discussion started: 12 March 2026

b) cross-correlation results and the associated lag per instrument, c) time series after synchronization. The vertical dashed bars indicate the original and final time stamps.

Adapted procedures are used for instruments that record at a time resolution other than 1 s. Pressure readings from the mSEMS are obtained at 1 s resolution. However, the first step of processing with the manufacturer software provides the aerosol number size distribution at a coarser resolution. The time resolution is between 1 and 3 minutes and depends on the number of bins and the measurement time per bin, which can vary between campaigns based on the ambient aerosol concentration and the trade-off between scanning time and counting statistics. We calculate the time lag from the raw mSEMS file and then apply it to the coarser resolution data.

For instruments that do not record pressure data, regardless of their time resolution, such as the CPC3007 (1 s resolution), the microAeth (1 min resolution) or the CO and O_3 sensors (1 and 2 s resolution, respectively), the internal clocks are regularly synchronized with the flight computer to ensure accurate alignment based on timestamps.

After all data are time synchronized, the local time might be converted to UTC, depending on the campaign, and the data from all instruments are merged into a single flight file.

4.1.3 Level 1 data processing

The objective of this step is to remove outliers, spurious data from instrument malfunction, and to apply all available data corrections from e.g., instrument intercomparisons and calibrations. Flight altitude is calculated with a barometric equation. The final step at this stage is the conversion of all data into standard temperature and pressure (STP) conditions. Hereafter, the different processing steps for each variable are described.

https://doi.org/10.5194/essd-2026-146
Preprint. Discussion started: 12 March 2026

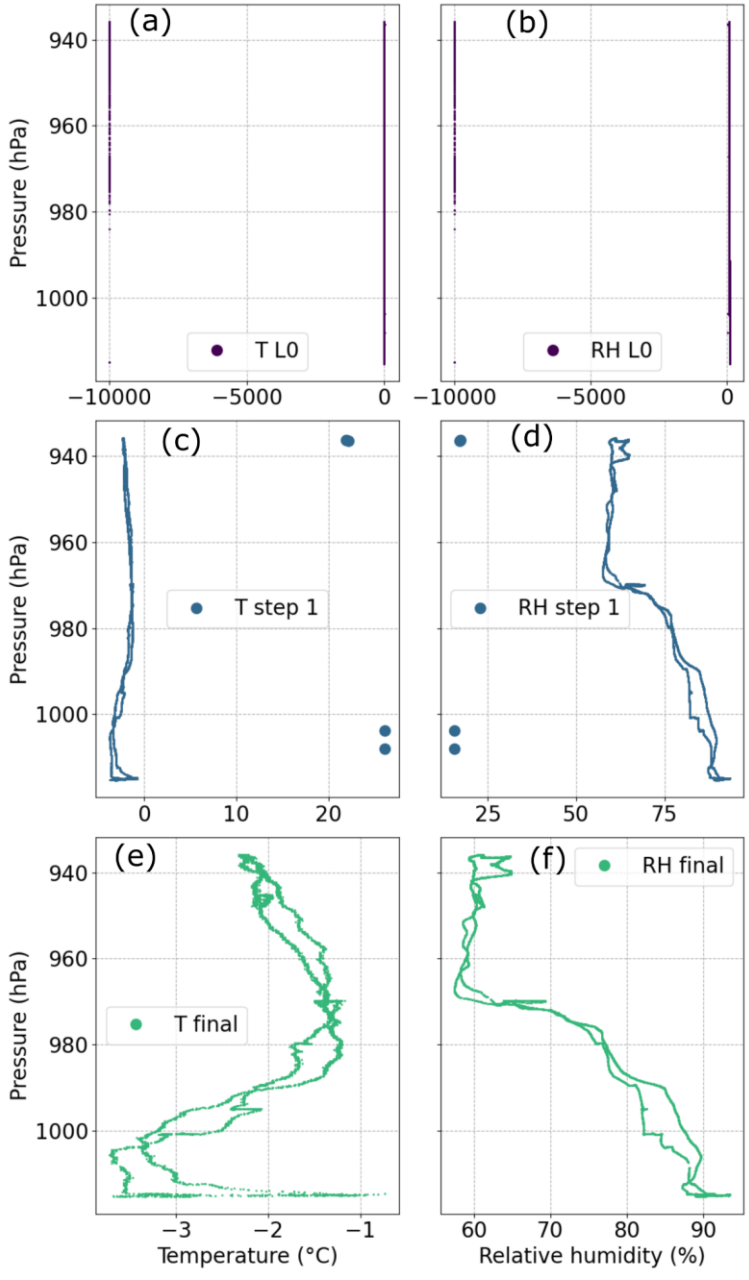

277

278 **Figure 5: Example of outlier removal for one flight profile during ARTofMELT on 3 June 2023. a, b) L0 data for T and RH; c, d)**
279 **data after removing obvious outliers outside reasonable range (here negative values); e, f) final L1 data after despiking and visual**
280 **inspection.**

281 **Temperature, relative humidity, pressure and altitude.** Obvious outliers are data points outside of the realistic range of
282 values for a given variable (e.g., negative relative humidity or temperature above 100 °C). Those data points are removed first
283 based on thresholds of realistic values. Less obvious outliers could be within the conceivable measurement range, but are only

https://doi.org/10.5194/essd-2026-146
Preprint. Discussion started: 12 March 2026

few data points with values different from the adjacent data points. They are identified by applying a despiking function, and by subsequent visual inspection by the data processor. The despiking function is based on a comparison between the raw measurements and the exponentially weighted moving average, with a 10 s window, which could be adjusted depending on the dataset (Patel and Divecha, 2010) to exclude differences higher than a defined threshold. Figure 5 illustrates the stepwise removal process of erroneous data. Panels a) and b) show the temperature and RH, respectively, with large negative values (-9999), which correspond to sensor or reading issues during sampling. After removal of these data points, the vertical structure of the temperature and RH profiles emerges, but a few remaining outliers can be easily identified (Fig. 5c and d). These outliers are removed with the dispiking function (Fig. 5e and f).

Once the temperature, pressure, and relative humidity data are processed, the flight altitude H can be calculated based on:

$$H = -\frac{P_0}{\rho_0 g} \times log\left(\frac{P}{P_0}\right) \quad \text{Eq. 1}$$

P_0 is the ground pressure, P is the observed pressure, g is the standard acceleration of gravity =9.807 m s^{-2}, and ρ_0 is the moist air density (WMO, 2025). An important point to consider is the evolution of ground pressure during a flight. If ground measurements of pressure are available, they are directly implemented in Eq.1 as P_0. If no ground pressure measurements were available for the duration of the flight, the average pressures before takeoff and after landing are considered as the ground reference, and a linear detrending function was applied for the EERL Helikite altitude to match before and after the flight on the ground.

Wind speed and direction. For the campaigns listed in Table 1, the SmartTether was deployed roughly 2 m below the MoMuCAMS and attached directly to the tether (Fig. 1). It provides direct measurements of wind speed and wind direction in the Earth's coordinate system. Outliers are identified and removed as for e.g., temperature data as described above.
More recently, a sonic anemometer was installed on MoMuCAMS and provided additional wind measurement. While it is not yet reported in any of the datasets described here, we provide details on the data processing for the future. The sonic anemometer provides wind measurements in the Helikite coordinate system, i.e., facing the wind direction. To retrieve the meteorological wind in the North-East coordinate system, positions and attitude angles of the MoMuCAMS were recorded by a VectorNav VN-200 Inertial Navigation System. The equations from Lenshow and Spyers-Duran (1989) were applied to get the wind speed and direction in the Earth's coordinate system.

Aerosol number size distribution from the mSEMS. Data from the mSEMS are reported as number size distribution (*dN/dlogDp*). From there the integrated particle number concentration is calculated and provided as total particle number concentration (lower and upper diameters can vary between campaigns). Data showing signs of instrument malfunction are identified. These include indications of i) overheating of the instrument (too high concentration for the small diameter bins only), ii) flooding of the optical chamber with butanol due to strong motions of MoMuCAMS (too large concentration in all

https://doi.org/10.5194/essd-2026-146
Preprint. Discussion started: 12 March 2026

size bins), or iii) low butanol levels in the condensation chamber (concentrations dropping towards zero). The corresponding data are excluded from the datasets. Potential size-shift and counting efficiency corrections, based on calibration data associated with a specific campaign, can also be carried out at this step if necessary.

Total particle number concentration from particle counters. For the aMCPC the same checks as for the mSEMS are carried out. Mostly it is part of the mSEMS set up. For the CPC3007 and the Partector 2, outliers corresponding to spurious values inconsistent with the adjacent data, such as unrealistically high concentrations, are identified and removed through visual inspection by the data processor (similarly to the example in Fig. 5). Counting efficiency corrections are carried out at this step if necessary and possible.

Aerosol number size distribution from the POPS. L0 POPS data is in units of particle counts per second and per bin. From there, the concentration in cm^{-3} is obtained by dividing the particle counts by the mean flow rate over the duration of the flight. Bins 1 to 3 corresponding to mean diameters of 149, 162, and 178 nm are excluded due to overcounting. A detailed explanation can be found in Pohorsky et al. (2024). The total particle number concentration for aerosol diameters between 186 nm and 3370 nm is determined as the sum of the remaining bins. The aerosol number size distribution in $dN/dlogD_p$ is derived by dividing the bin concentrations by $dlogD_p$ (with D_p as the midpoint diameter of each bin). Data showing signs of instrument malfunction are identified and excluded. These include indications of i) temporary decrease in the pump flow (concentrations dropping towards zero) or ii) spurious values inconsistent with the adjacent measurements (unrealistically high or low concentrations in all size bins). Potential diameter size-shift and counting efficiency corrections, based on calibration data associated with a specific campaign, can also be carried out at this step if necessary.

Cloud droplet number size distribution from the miniCDA. The cloud droplet number concentration is obtained by dividing the bin counts that are provided at L0 by the mean flow rate over the duration of a flight. Bins 1 to 71, corresponding to midpoint diameters between 0.24 and 0.66 µm, are excluded as they fall below the instrument's detection limit. The total droplet concentration is then obtained by summing the concentrations from bins 72 to 256. Similarly to aerosol concentrations, the counts are converted into a $dN/dlogD_p$ size distribution. Counting efficiency and size corrections could be implemented at this step, if intercomparison data with standard instruments are available.

CO_2. Raw measurements are directly corrected for temperature variations with an internal temperature sensor but need to be corrected for pressure variations. The conversion to standard pressure is described at the end of this section. After this correction, the mixing ratio is further converted to a dry mole fraction, using the ambient relative humidity measurements. A calibration factor also needs to be applied. The calibration factor is obtained from lab experiments with specific CO_2 mixing ratios using a linear regression between the observed and calibration gas CO_2 mixing ratios. Finally, data are visually inspected for outliers (i.e., unrealistic values), which are flagged and removed.

https://doi.org/10.5194/essd-2026-146
Preprint. Discussion started: 12 March 2026

CO. The CO data at L0 are provided as dry mixing ratios in standard temperature and pressure (STP). They are corrected by removing the instrument's measured baseline. The baseline is obtained through operating the CO scrubber 30 min before and after the flight. A linear interpolation of this baseline is applied to account for changes between the beginning and the end of each flight. It is then subtracted from the L0 measurements of CO. Data processing includes a visual quality inspection and removal of outliers similarly to the other data products.

O_3. L0 O_3 measurements are reported in STP and dry mixing ratios. Using an ozone scrubber, a zero calibration is carried out in each campaign and the dry mixing ratios may be corrected for an offset. The resulting ozone data are visually inspected for outliers that are removed like for the other data products.

Aerosol absorption properties from the STAP and microAeth. For the STAP measurements, a 2-min moving average has already been applied during the pre-processing step described in Sect. 4.1.1. The absorption coefficients of L0 are inspected for outliers, such as spurious values inconsistent with the adjacent data, which are removed. In certain situations, when coefficient values are low and a rapid change of ambient relative humidity occurs, data become very noisy or can even display negative values. These data are considered faulty and are removed.
The microAeth provides eBC concentration data. Values below detection limit and positive outliers are removed. In addition, absorption coefficients at each wavelength can be derived from the eBC concentrations using the wavelength-dependent mass absorption cross sections (MACs) provided by AethLabs (7.78, 10.84, 13.10, 14.67, and 18.52 $m^2\ g^{-1}$ at 880, 625, 528, 470 and 375 nm, respectively). More details of the instrument and calculation approach are provided in Alden et al. (2025b).

Standard Temperature and Pressure correction. After the above processing steps, all data, which were not reported in STP, are converted to standard conditions. The following equation is used:

$$x_{STP} = x \times \frac{T}{T_0} \times \frac{P_0}{P} \qquad \text{Eq. 2}$$

With x the measurements to correct, and x_{STP} is the STP corrected values. T and P are the temperatures in K and the pressures in hPa observed for every x during the flight. T_0 is 273.15 K and P_0 equals 1013.25 hPa.

4.1.4 Level 1.5 data processing

At this stage, only the scientifically relevant variables are retained for the final dataset (i.e., houskeeping variables e.g., internal temperature, flow rate, or laser power variables are removed). The column names are standardized to ensure consistency across different campaigns. Data recorded before takeoff and after landing are also excluded, keeping only the measurements relevant to the flight. In addition, three flags are added to the datasets to facilitate the scientific analysis of the EERL Helikite measurements, and information on the flight number and campaign name is included for reference.

https://doi.org/10.5194/essd-2026-146
Preprint. Discussion started: 12 March 2026


Open Access Earth System Science Data Discussions

The "flag_pollution" identifies periods when the data are affected by local pollution, e.g., fossil fuel emissions from a ship stack during ARTofMELT or local activities at the observatories during CLAVIER and ORACLES. When pollution is part of the measured environment and aligned with the campaign objectives, it is not flagged, as it represents a relevant component of the observations as e.g., in ALPACA. For ARTofMELT, pollution was detected near the stack height by the POPS, the STAP, and the mSEMS, which showed a pronounced Aitken mode. During CLAVIER, local pollution was identified using the POPS and mSEMS, again showing a distinct Aitken mode. For ORACLES, local pollution was visible in the CPC3007 data and confirmed using the flight notes. In contrast, during ALPACA and CHOPIN, local pollution was part of the study objectives, and no specific pollution flag was applied in that dataset. When "flag_pollution" is set to 1, pollution is present.

The second flag, "flag_hovering" is applied when the EERL Helikite is stationary, i.e., remaining at constant altitude (within ± 10-20 m, depending on the flight) for a period exceeding 2 minutes. If "flag_hovering" is set to 1, hovering occurs. On the one hand, hovering information is important when performing data averaging, temporally or spatially, because the number of data points per altitude is strongly impacted. On the other hand, hovering is necessary for certain types of observations, e.g., for filter sampling, to increase the counting statistics from low time resolution instruments such as the mSEMS, and if a scientifically interesting feature is observed (e.g., cloud, pollution plume) or for technical reasons. To accommodate the coarser time resolution for particle number size distributions from the mSEMS, flight patterns typically include a step-wise ascent or descent to improve counting statistics at different altitudes. This flag can hence be used to more easily select data to refine the analysis of data with a coarser resolution for instance.

The third flag, "flag_cloud" informs about cloud conditions. "flag_cloud" is set to 1, when measurements are conducted in cloud or fog and 0 otherwise. For example, in the ARTofMELT campaign, clouds were identified based on aerosol data, high relative humidity, videos and flight notes, as well as ceilometer and cloud radar data providing cloud base height and reflectivity information. During CLAVIER, cloud periods were flagged using aerosol data and RH. For ORACLES, clouds were primarily identified from the miniCDA data and when unavailable, aerosol data and RH were used together with the camera footage. In CHOPIN, the flag was based on flight notes, camera footage, and miniCDA data, while for PaCE, cloud presence was determined from remote sensing and RH data. Note that defining the presence of a cloud is inherently difficult due to rapidly changing conditions, patchy clouds or multiplayer clouds. In addition, the same measurements are not always available. The cloud flag should therefore be considered with caution.

At the end of Level 1.5, a 1 s resolution file is produced for each flight.

https://doi.org/10.5194/essd-2026-146
Preprint. Discussion started: 12 March 2026

4.1.5 Level 2 data processing

Data are averaged to 10 seconds. This averaging period is selected to keep the high-resolution information, while removing noisy signals resulting from low concentrations, the platform motions or the sensitivity of the instruments. Once all flights have been processed and averaged to 10 second resolution, the individual flight files are merged into a single final campaign dataset.

Table 3: Variables provided in the data products and key processing steps at all levels

Variable name (column header in data product)	Unit	Raw data and Level 0 comment	Level 1 comment	Level 2 comment
Altitude	m	n.a.	Calculated using barometric equation (Eq. 2) 1 s resolution Quality control (QC)	10 s averaged
Latitude (Lat)	deg	Time synchronization with cross correlation (Eq. 1) Then all variables merged directly into L0 file with 1 s resolution	QC	10 s averaged
Longitude (Long)	deg			
Pressure (P)	hPa			
Temperature (Temperature)	°C		QC Average from 2 sensors for each variable	10 s averaged
Relative humidity (RH)	%			
Wind speed (WindSpeed)	m s^{-1}		QC	10 s averaged
Wind direction (WindDir)	deg			
CO_2 mixing ratio (CO2)	ppm		corrected + STP + QC	10 s averaged
Total particle number concentration $N_{186\text{-}3370}$ (POPS_total_N)	cm^{-3}		Apply correction factors + QC + STP	10 s averaged
POPS bin concentration (POPS_bX)	cm^{-3} (dN/dlogDp)			
Total droplet number concentration $N_{0.66\text{-}43}$ (mCDA_total_N)	cm^{-3}		QC + STP	10 s averaged
miniCDA bin concentration (mCDA_dataBX)	cm^{-3} (dN/dlogDp)			
Filter sampling (Filter_position)	-		n.a.	10 s averaged
Filter flow (Filter_flow)	lpm			

https://doi.org/10.5194/essd-2026-146
Preprint. Discussion started: 12 March 2026

Total particle number concentration $N_{10\text{-}1000}$ (CPC_total_N)	cm^{-3}	No pressure reading. Data merging based on manual time synchronization (pre-flight clock synchronization) into L0 file with 1 s resolution	Apply correction factors + QC + STP	10 s averaged
Total particle number concentration $N_{8\text{-}250}$ (mSEMS_total_N)	cm^{-3}	Time synchronization with cross correlation (Eq. 1) at raw data level Treatment of raw data with manufacturer software Then variables merged directly into L0 file with x min resolution	Apply correction factors + QC + STP	3 min resolution
mSEMS bin concentration (mSEMS_Bin_ConcX)	cm^{-3} (dN/dlogDp)			
Aerosol light absorption coeff. 450 nm (STAP_sigmab_smth)	Mm^{-1}	Time synchronization with cross correlation (Eq. 1) at raw data level Treatment of raw data with manufacturer software Then variables merged directly into L0 file with 1 s resolution	QC + STP	10 s averaged
Aerosol light absorption coeff. 525 nm (STAP_sigmag_smth)	Mm^{-1}			
Aerosol light absorption coeff. 624 nm (STAP_sigmar_smth)	Mm^{-1}			
MicroAeth eBC mass value for 375, 470, 528, 625, 880 nm (MA_eBC_X)	ng/m^3	No pressure reading. Data merging based on manual time synchronization (pre-flight clock synchronization) into L0 file with 1 min resolution	QC + STP	10 s averaged
MicroAeth light absorption coeff. 375, 470, 528, 625, 880 nm (MA_Abs_Coeff_X)	Mm^{-1}			
O_3 mixing ratio (O3)	ppb	Time synchronization with cross correlation (Eq. 1) Then variable merged directly into L0 file with 2 s resolution	Apply correction factors + QC + STP (automatic)	10 s averaged
CO mixing ratio (CO)	ppb	No pressure reading. Data merging based on manual time synchronization (pre-flight clock synchronization) into L0 file with 1 s resolution	Apply correction factors + QC + STP (automatic)	10 s averaged

https://doi.org/10.5194/essd-2026-146
Preprint. Discussion started: 12 March 2026

4.2 Example analyses

The purpose of this section is to provide examples of how data might be visualized and analyzed by the community. We do not provide extensive scientific interpretation, which can be found in campaign specific publications.

4.2.1 Vertical profiles of particle number concentrations

We present example vertical profiles of particle number concentrations between 186 and 3370 nm, measured with a POPS, and between 8 and 280 nm, measured with an mSEMS, from three different campaigns (Fig. 6). During the ARTofMELT expedition, 23 flights were carried out over the Arctic sea ice during the melt onset in May-June 2023. In a southern Greenlandic fjord system, during GreenFjord, 24 flights were performed between June and July 2023 (Alden et al., 2025). Finally, 19 flights were conducted during the Pallas Cloud Experiment (PaCE) in September-October 2022 in the boreal forest of Finland. Focusing on the larger accumulation and coarse mode, number concentrations vary between 10 and 100 cm^{-3} over the Arctic sea ice (Fig. 6a) and in the boreal forest (Fig. 6c), and occasionally drop below 10 cm^{-3} in the central Arctic. The individual profiles show situations with vertically homogeneously distributed aerosol concentrations and also stratified situations, where concentrations either decrease or increase with altitude. Observations in southern Greenland in summer (Fig. 6b) are, however, different. They are generally higher compared to the other two campaigns, ranging from 100 to 3000 cm^{-3}, most likely because of the proximity to the open ocean and sea spray generation. On specific occasions, concentrations increased with altitudes owing to three long-range transport events of biomass burning emissions from Canada at elevated altitudes (Alden et al., 2025b) as can be seen from the markers of individual flights. The fine mode particle vertical profiles (Fig. 6e-g) generally resemble the coarse mode profiles at each site. Surface concentrations are however higher and range from roughly 10 to almost 1000 cm^{-3} in the central Arctic (ARTofMELT). Over the boreal forest (PaCE), concentrations are similar but occasionally exceed 1000 cm^{-3}, while in southern Greenland they often exceed 1000 cm^{-3}.

https://doi.org/10.5194/essd-2026-146
Preprint. Discussion started: 12 March 2026

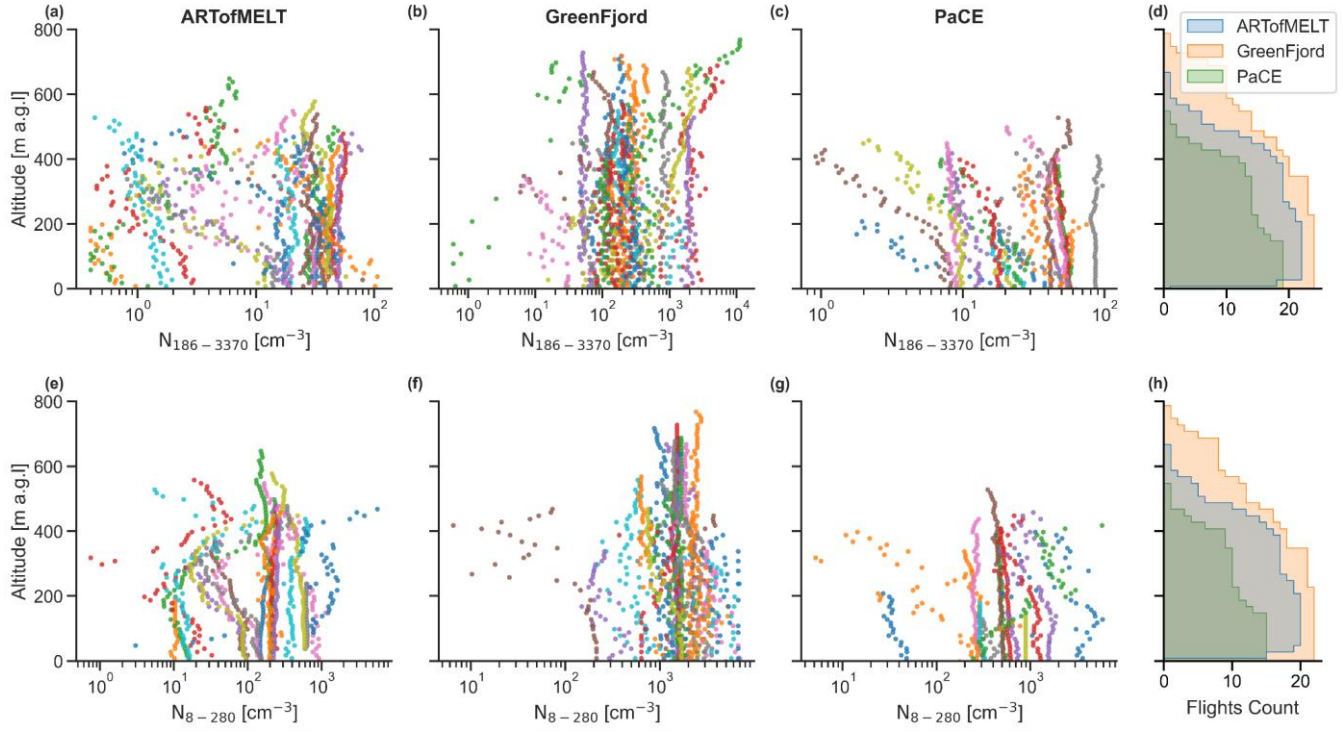

Figure 6: Vertical profiles of particle number concentrations from the ARTofMELT (a, e), GreenFjord (b, f) and PaCE (c, g) campaigns. The top row shows particle number concentrations between 186 and 3370 nm measured by a POPS. The bottom row displays the number concentration of particles between 8 and 280 nm measured by an mSEMS. The colored dots represent individual flights in each campaign and data are averaged per 10 m altitude. Panels d and h provide the number of flights for which data were recorded at specific altitudes.

4.2.2 Particle number concentrations relative to inversion heights

The recorded temperature profiles allow for the determination of inversions and investigation on how aerosols are transported across inversions. We provide examples on the role of surface-based inversions in the presence (ALPACA) and absence (CLAVIER) of surface aerosol sources (Fig. 7). In this example, surface-based inversions were determined by identifying the height where $dT/dz = 0$ as in Kahl (1990). The height of the top of the surface-based inversion was defined as 0.5 and data from each flight at altitudes below were normalized between 0 and 0.5, and between 0.5 and 1 for observations above the inversion top. In the urban winter environment of Fairbanks, Alaska (panel a, ALPACA), the aerosol number concentration below the surface-based inversion top (dashed horizontal line) is significantly higher than above. Below the inversion the vertical profiles exhibit a decrease from the surface upward which is expected since the surface emissions can only slowly be mixed upward. Above the inversion, aerosol number concentrations reach their minimum values reflecting a type of background concentration with little influence from surface emissions (Pohorsky et al., 2025b). The observations during CLAVIER in northern Greenland are different. Below the inversion the particle number concentrations are lower due to the absence of surface sources, while above the inversion, concentrations tend to be higher due to long-range transport of mid-

https://doi.org/10.5194/essd-2026-146
Preprint. Discussion started: 12 March 2026

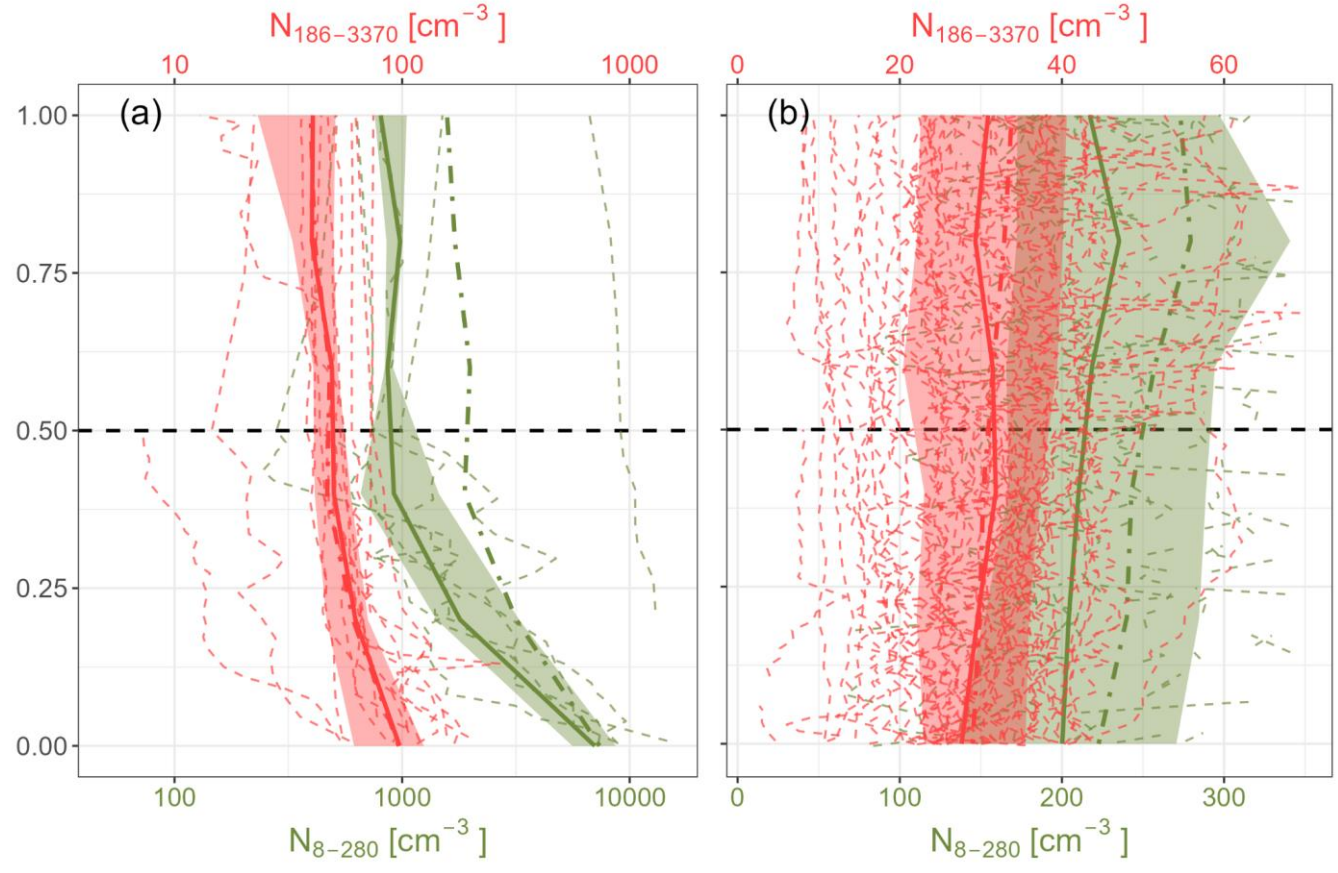

Figure 7: Vertical profiles of particle number concentrations normalized to the surface-based inversion height at 0.5 for a) the urban winter atmosphere of Fairbanks (ALPACA, n=10), and b) a remote high Arctic site during spring (CLAVIER, n=51). For both panels, the full line represents the median of all individual profiles, the shading indicates the interquartile range and the dashed lines represent the mean.

4.2.3 Aerosol properties below, in and above clouds

In Fig. 8 we illustrate one possible approach to using the cloud flag described in Sect. 4.1.4 by normalizing the vertical profiles of particle number concentrations to the cloud base height and cloud top. During the ARTofMELT expedition there were two distinct types of aerosol vertical profiles when clouds were present and the EERL Helikite was also able to conduct measurements above the cloud. One type (orange profile, flight on June 7th, 2023) featured very low particle number concentrations below cloud, i.e., around a 100 cm^{-3} for the fine mode, and around 10 cm^{-3} for the coarse mode, while above

https://doi.org/10.5194/essd-2026-146
Preprint. Discussion started: 12 March 2026

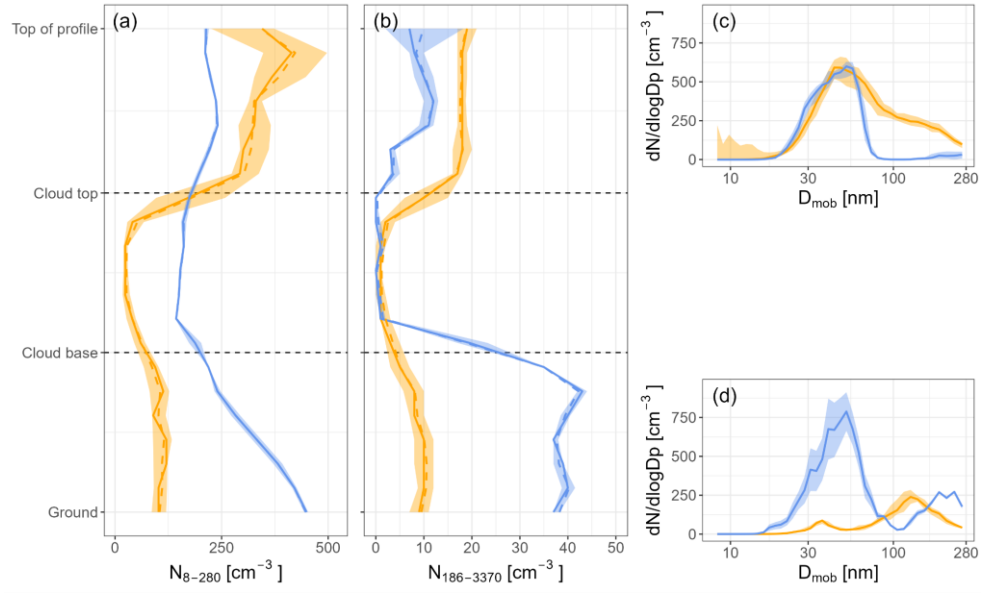

Figure 8: Comparison of two vertical profiles normalized to cloud base height during the ARTofMELT campaign on June 7th, 2023 (orange) and June 10th, 2023 (blue). a) Total aerosol concentration between 8 and 280 nm measured with the mSEMS. b) Total aerosol concentration between 186 and 3370 nm measured with the POPS. Normalization means that the vertical extent of each observation category (i.e., below, within and above cloud) is represented as one third of the profile. c) Particle number size distributions above the cloud. d) Particle number size distributions below the cloud. For all panels, the full line represents the median of all individual profiles, the shading indicates the interquartile range and the dashed lines represent the mean.

5 User guidance

Here we provide considerations for users of these, and future, EERL Helikite datasets. Tethered-balloon data offer the possibility to visualize the vertical distribution of the different variables as illustrated above. Fast profiles provide a quasi-snapshot of the state of the vertical column. However, flights typically include "hovering" periods where the EERL Helikite

https://doi.org/10.5194/essd-2026-146
Preprint. Discussion started: 12 March 2026

is maintained at a constant altitude. Under these conditions, more data points are collected at a given altitude but the measurements are subject to local and temporal variability (e.g., from eddies or horizontal advection). Additionally, the advection of sporadic features such as a small cumulus cloud or a pollution plume can sometimes be captured very briefly while profiling. Because of the very sporadic nature of these features, their full vertical extent may not always be fully captured. For an analysis of the vertical structure of the atmosphere, it is therefore recommended to first observe the flight pattern (i.e., altitude versus time) to identify fast profiles and hovering periods to select flight segments appropriate for the intended analysis, and to spatially average the data (e.g., in vertical layers of 10 m as in Fig. 4, or levels corresponding to a model output). Hovering periods, defined by the "flag_hovering" in the datasets, are useful to obtain better counting statistics from instruments with coarser time resolution (e.g., mSEMS) to evaluate variations between different atmospheric layers or to compare the temporal evolution of a specific variable at a specific altitude. Information on local pollution that might affect the aerosol measurements is also included in the datasets with the "flag_pollution" and should be considered and removed if not desired. In addition, it is recommended to make use of ancillary data such as from ground-based remote sensing that is frequently available (e.g., ceilometer observations during Greenland or CloudNet during ORACLES).

The aerosol inlet of MoMuCAMS can be considered as interstitial inlet due to its horizontal orientation and generally low flow rate between 0.54 and 3 lpm (compared to standard ground-based monitoring stations) with a 7.5-mm inner diameter. In clouds, water droplets are not captured by the inlet. Consequently, measurements usually show an apparent depletion of aerosols inside clouds, and only interstitial particles remain visible. It is possible that very small droplets are still captured by the inlet and measured. However, since the inlet is heated, those might evaporate in the inlet. The transmission of the very small droplets depends hence on the flow rate of the system and can therefore change from one flight to another.

Relative humidity measurements typically show higher uncertainties at elevated RH (> 90 %). We also observe that RH does not always reach 100 % in clouds. Both temperature and RH measurements are subject to ground effects (e.g., from excessive heating of the surface from solar radiation). Despite careful data cleaning, data points near the ground should always be treated with care, especially if a spatial data averaging is applied.

6 User resources and code availability

All data were processed in Python with the EASE code. The code package is available on Github: https://github.com/EERL-EPFL/helikite-data-processing.

A Python Jupyter Notebook script is available: https://github.com/EERL-EPFL/helikite-data-processing/blob/main/notebooks/ESSD_Plot_Helikite_level2.ipynb to support the initial handling of the datasets and to produce quick-looks of the EERL Helikite flights. The software provides different visualization functions for each of the datasets:

https://doi.org/10.5194/essd-2026-146
Preprint. Discussion started: 12 March 2026

a) Vertical profiles for each flight for each variable. Each flight is subdivided into ascent and descent based on the maximum altitude reached during the flight. Flags are included as shaded areas.
b) Time series for each flight for each variable. A dotted line marks the transition between ascent and descent. Flags for cloud presence, pollution, and stationary flight, are displayed as well.
c) Average profile: for each variable, an average profile is obtained from all the profiles of the campaign.
d) Overview of the campaign: all the profiles of the campaign are plotted and color coded based on the flight number.

See Appendix A for examples.

7 Summary

In this data descriptor we provide information on the processing from raw to level 2 data, following recommendations from EBAS for data levels for 15 different instruments typically deployed on the EERL Helikite. The specifically developed Python code EASE is used for this purpose and available on Github. We further provide a quick look plotting tool that users can apply to explore the EERL Helikite data. To guide the exploration of the data, examples are given on how data can be visualized and analyzed for specific purposes such as aerosol dispersion across temperature inversions or aerosol-cloud interactions. The data can be used e.g., for model and remote sensing validation or as contextual information of vertical aerosol profiles at the given locations and seasons for future measurements there that do not dispose of vertical observational facilities. For most of the campaigns mentioned in this data descriptor, specific manuscripts have been published or are in preparation. Nevertheless, the datasets are rich in information and it requires the wider research community to fully take advantage of the vertical aerosol information in the lower atmospheric boundary layer in polar and alpine regions. More data will be added from future campaigns and updates on the availability of new data sets can be obtained here: https://www.epfl.ch/labs/eerl/eerl-home-page/research/field-work-overview/.

https://doi.org/10.5194/essd-2026-146
Preprint. Discussion started: 12 March 2026

Data availability

All data described above are available here:

1. ARTofMELT: Pohorsky et al. (2025), https://bolin.su.se/data/oden-artofmelt-2023-aerosols-vertical
2. ALPACA: Pohorsky et al. (2025a), https://arcticdata.io/catalog/view/doi%3A10.18739%2FA2MS3K363
3. Brigerbad: Schmale et al. (2026), https://zenodo.org/records/18327462
4. CHOPIN: Alden et al. (2026), will be available on the ACTRIS homeless data portal: https://dc.actris.nilu.no/search
5. CLAVIER: Calmer et al. (2026), will be available on the ACTRIS homeless data portal: https://dc.actris.nilu.no/search
6. GreenFjord: Alden et al. (2025a), https://zenodo.org/records/15387480
7. ORACLES: Temel et al. (2026b), https://zenodo.org/records/18664026
8. PaCE: Lonardi et al. (2026), https://zenodo.org/records/18663940
9. Turtmann: Temel et al. (2026a), https://zenodo.org/records/18327709

Author contributions

JS, RP, YT, ML, JA, RC wrote the manuscript. RP, JA, RC, YT, ML, OS, ET, AS wrote data processing code. RP, JA, RC, YT, ML, NB, BH, AB, MLH, RP, OS, AT, HH processed and curated data. All authors contributed to creating the final data sets and commented on the manuscript.

Competing Interests

The authors declare that they have no conflict of interest.

Special issue statement

This article is part of the special issue:" Data generated during the Pallas Cloud Experiment 2022 campaign".

Acknowledgements

We would like to acknowledge numerous colleagues for their support during each of the field campaigns, specifically for providing facilities, helping with the EERL Helikite deployment and supporting flight permit applications. In no specific order we would like to thank: the team of the ARTofMELT campaign as well as the Swedish Polar Research Secretariat and the Oden crew; the ALPACA team and the University of Fairbanks; the municipality of Brigerbad; the CHOPIN team, the University of Demokritos, and the Kalavrita Ski Resort Operators; the CLAVIER team and the Department of Environmental Science, Aarhus University is acknowledged for providing logistics at Villum Research Station in North ; the GreenFjord team,

https://doi.org/10.5194/essd-2026-146
Preprint. Discussion started: 12 March 2026

the Narsaq International Research Station and the residents as well as municipality of Narsaq; the Neumayer Station Crew and the Alfred Wegener Institute; the PaCE team and David Brus from the Finish Meteorological Institute; and Gabriel Ammann and the municipality of Turtmann.

JS holds the Ingvar Kamprad Chair for Extreme Environments Research sponsored by Ferring Pharmaceuticals.

Financial support

We acknowledge funding from the Swiss National Science Foundation (grant numbers TMCG-2_213771, 200021_212101, 200021_188478, IZSEZ0_233702), the Swiss Polar Institute (grant numbers SPI-FLAG-2021-002 Greenfjord, and Technogrants 2019 MoMuCAMS, 2023 MAMS, 2024 ATB), as well as the European Union's Horizon 2020 research and innovation program under grant agreement no. 101003826 via project CRiceS (Climate Relevant interactions and feedbacks: the key role of sea ice and Snow in the polar and global climate system) and under grant agreement no. 101137639 for CleanCloud (Clouds and climate transitioning to post-fossil aerosol regime), a Horizon Europe Cluster 5 project. We further received support from ACTRIS ATMO-ACCESS TNA 2022-0000000098.

https://doi.org/10.5194/essd-2026-146
Preprint. Discussion started: 12 March 2026

Open Access Earth System Science Data Discussions

Appendix A

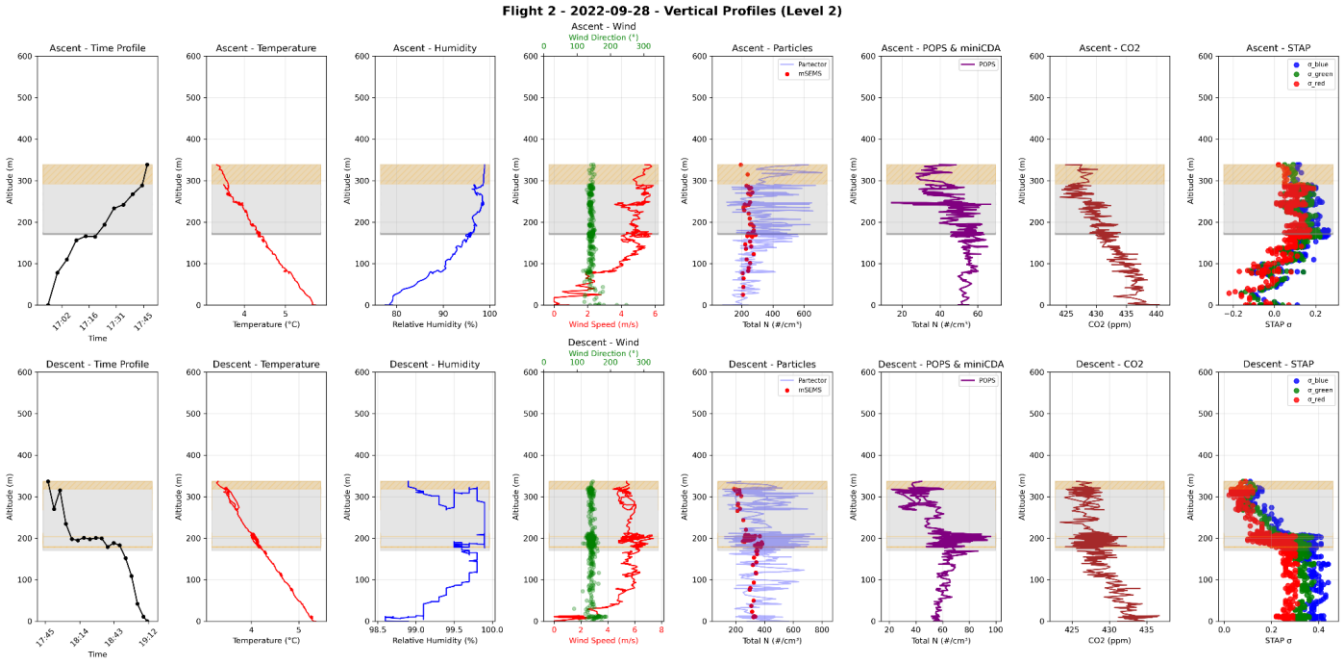

Figure A1. Vertical profiles of all variables for one example flight (flight 2 of PaCE). The upper panels display the ascent profile, and the bottom panels the descent profile. In each panel, the presence of a cloud is indicated by a gray shading based on the cloud flag. A yellow shading indicates a stationary period lasting more than 2 minutes, based on the hovering flag. The first panel indicates the altitude of the balloon resampled every 5 minutes to ease the reading. The second and third panels indicate temperature and relative humidity. The fourth panel combines wind speed (red, bottom x-axis) and the wind direction (green, upper x-axis). The fifth panel indicates the total concentrations of sub-micron particles, displaying measurements by mSEMS (red), Partector (blue), CPC (green, not flown). The next panel showcases the number concentrations of larger particles and droplets with measurements from the POPS (purple) and miniCDA (yellow, not flown). The seventh panel indicates the mixing ratio of CO2. The last panel indicates the absorption coefficients of the STAP or microAeth, data are color-coded based on the wavelength.

https://doi.org/10.5194/essd-2026-146
Preprint. Discussion started: 12 March 2026

Open Access Earth System Science Data Discussions

589

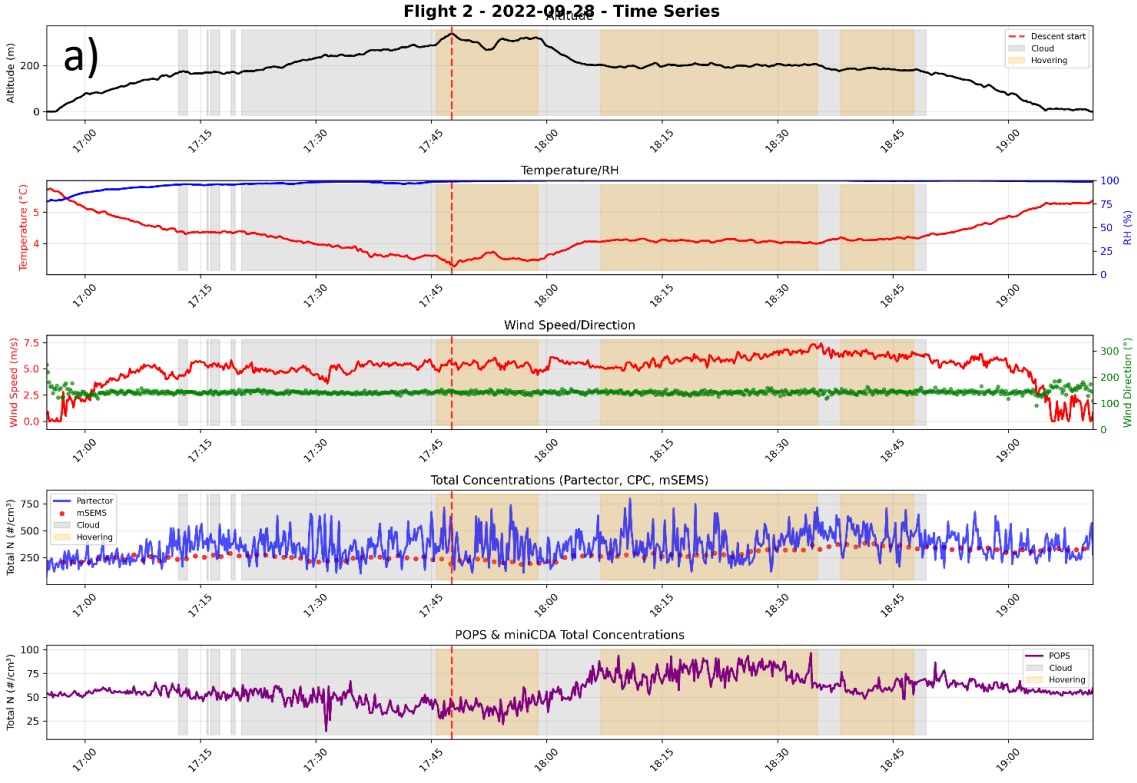

590

591

https://doi.org/10.5194/essd-2026-146
Preprint. Discussion started: 12 March 2026

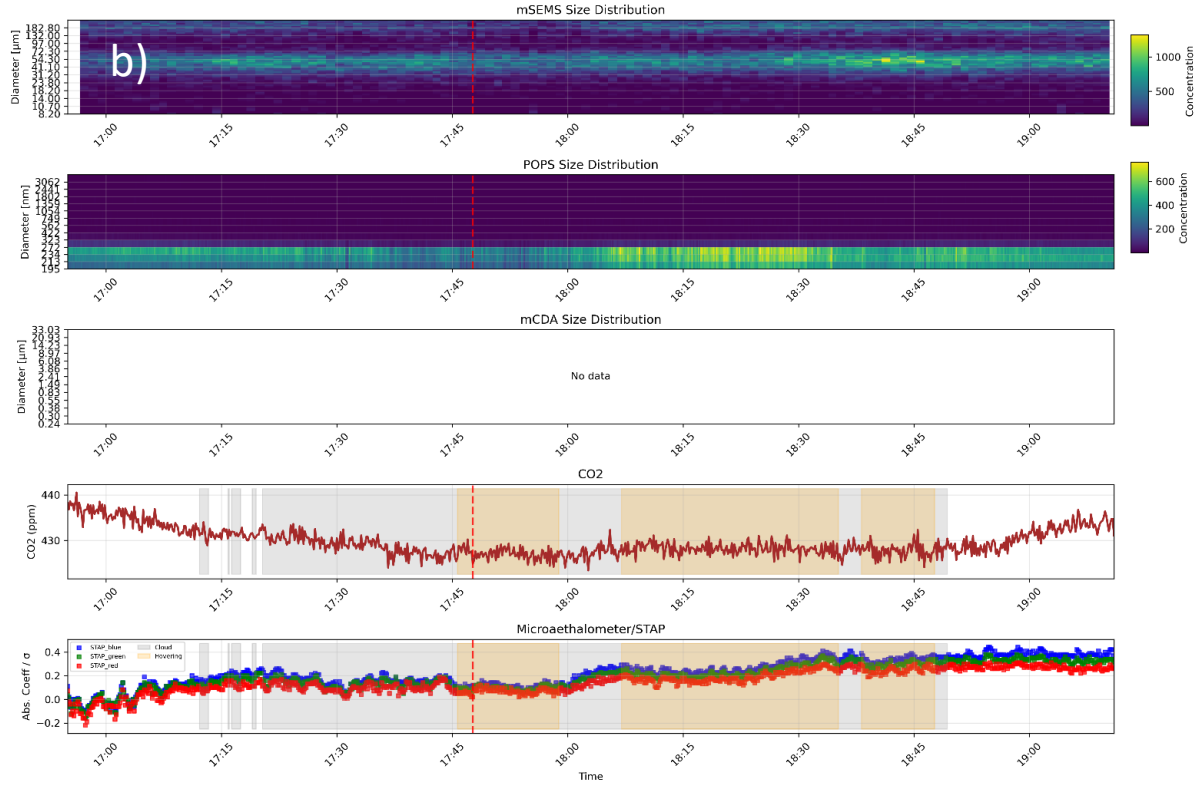

Figure A2. Time series from flight 2 of PaCE. The temporal evolution of selected variables is displayed in 10 stacked panels (here separated into panels a and b) following the same time axis. A red dashed line separates the ascent from the descent. Flags for clouds, stationary flight, are displayed as shaded areas. The first panel indicates the altitude of the profile. The second panel combines temperature (red, left y-axis) and relative humidity (blue, right y-axis). Wind speed (red, left y-axis) and wind direction (green, right y-axis) are shown in the third panel. Panel 4 displays the total concentration of sub-micron particles, with data from mSEMS (red), Partector (blue), and CPC (green, not flown). Similarly, the fifth panel features the total concentration of larger particles by the POPS (purple) and droplets by the miniCDA (yellow, not flown). Panels 6 to 8 display heatmaps of the size distributions by mSEMS, POPS, and miniCDA. The left axes indicate the mid-diameter of some of the bins, while individual colorbars are provided on the right side of the panels. Panel 9 indicates the CO_2 concentration. The last panel indicates the absorption coefficient of STAP of microAeth, with color-coding based on the wavelength.

https://doi.org/10.5194/essd-2026-146
Preprint. Discussion started: 12 March 2026

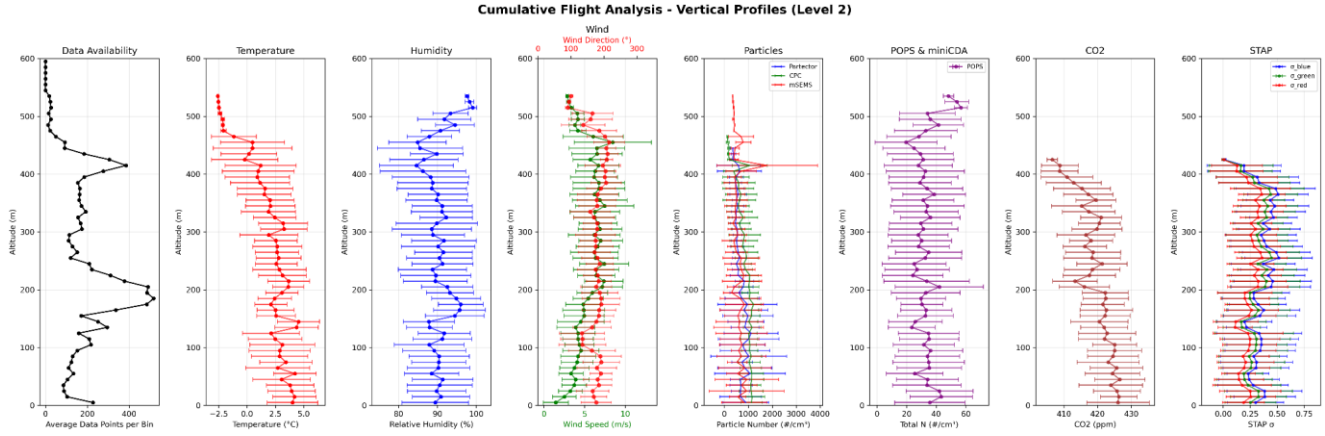

Figure A3. Vertical profiles of averaging all helikite data from the PaCE campaign. This figure is obtained by combining the ascents and descents of all the flights, binning data every 10 m of altitude. Panel 1 indicates the average number of points per bin. All other panels 2-8 are structured as in figure A1. a solid line indicates the average, horizontal bars indicate the standard deviation.

https://doi.org/10.5194/essd-2026-146
Preprint. Discussion started: 12 March 2026

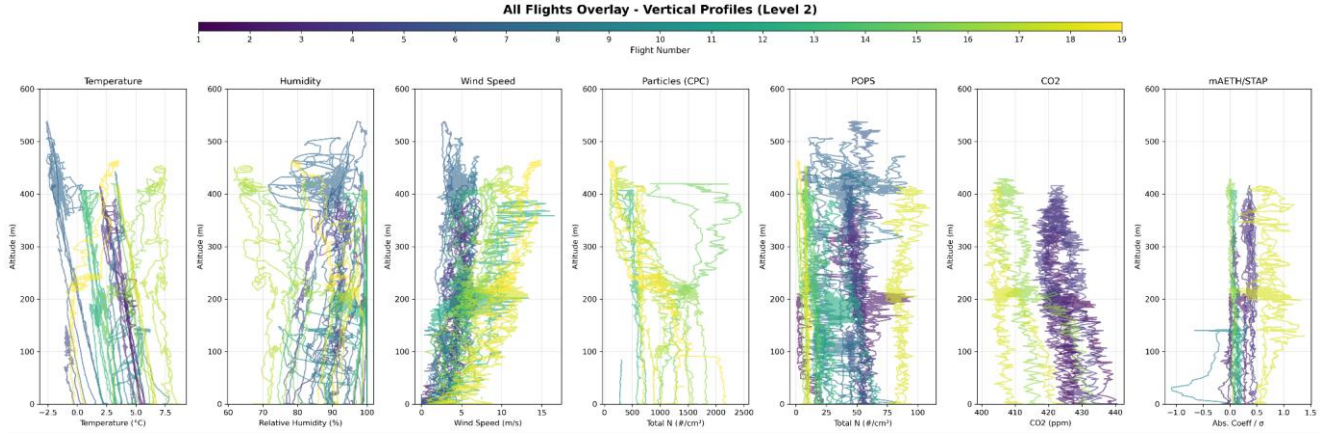

Figure A4. Overview of all vertical profiles from the PaCE campaign. The figure is obtained by combining all the vertical profiles, and color coding them based on the flight number. The color variation represents the – non-normalized - temporal evolution of the campaign.

https://doi.org/10.5194/essd-2026-146
Preprint. Discussion started: 12 March 2026

References

Alden, J., Bergner, N., Heutte, B., Favre, L., Weng, J., Violaki, K., and Schmale, J.: Vertical aerosol, trace gas and weather data taken with a tethered balloon system in summertime in Narsaq, South Greenland during Greenfjord 2023, https://doi.org/10.5281/zenodo.15387480, 2025a.

Alden, J., Bergner, N., Heutte, B., Favre, L., Surdu, M., Weng, J., Augugliaro, M., Winiger, P., Dönmez, B., Pohorsky, R., Calmer, R., Chatterjee, C., Violaki, K., Nenes, A., Gregor, L., Henning, S., and Schmale, J.: Vertically-resolved source contributions to climate-relevant aerosol properties in Southern Greenlandic fjord systems, EGUsphere, 1–43, https://doi.org/10.5194/egusphere-2025-5710, 2025b.

Alden, J., Helmig, H., Lonardi, M., Temel, Y., Heutte, B., Pohorsky, R., Favre, L., and Schmale, J.: Aerosol and meteorological data from a tethered balloon during the CHOPIN campaign Oct-Nov 2024 at Mt. Helmos, Greece (0), 2026.

Altstädter, B., Platis, A., Wehner, B., Scholtz, A., Wildmann, N., Hermann, M., Käthner, R., Baars, H., Bange, J., and Lampert, A.: ALADINA – an unmanned research aircraft for observing vertical and horizontal distributions of ultrafine particles within the atmospheric boundary layer, Atmospheric Measurement Techniques, 8, 1627–1639, https://doi.org/10.5194/amt-8-1627-2015, 2015.

Ansmann, A., Ohneiser, K., Engelmann, R., Radenz, M., Griesche, H., Hofer, J., Althausen, D., Creamean, J. M., Boyer, M. C., Knopf, D. A., Dahlke, S., Maturilli, M., Gebauer, H., Bühl, J., Jimenez, C., Seifert, P., and Wandinger, U.: Annual cycle of aerosol properties over the central Arctic during MOSAiC 2019–2020 – light-extinction, CCN, and INP levels from the boundary layer to the tropopause, Atmospheric Chemistry and Physics, 23, 12821–12849, https://doi.org/10.5194/acp-23-12821-2023, 2023.

Asmi, A., Collaud Coen, M., Ogren, J. A., Andrews, E., Sheridan, P., Jefferson, A., Weingartner, E., Baltensperger, U., Bukowiecki, N., Lihavainen, H., Kivekäs, N., Asmi, E., Aalto, P. P., Kulmala, M., Wiedensohler, A., Birmili, W., Hamed, A., O'Dowd, C., Jennings, S. G., Weller, R., Flentje, H., Fjaeraa, A. M., Fiebig, M., Myhre, C. L., Hallar, A. G., Swietlicki, E., Kristensson, A., and Laj, P.: Aerosol decadal trends-Part 2: In-situ aerosol particle number concentrations at GAW and ACTRIS stations, Atmospheric Chemistry and Physics, 13, 895–916, 2013.

Bates, T. S., Quinn, P. K., Johnson, J. E., Corless, A., Brechtel, F. J., Stalin, S. E., Meinig, C., and Burkhart, J. F.: Measurements of atmospheric aerosol vertical distributions above Svalbard, Norway, using unmanned aerial systems (UAS), Atmos. Meas. Tech., 6, 2115–2120, https://doi.org/10.5194/amt-6-2115-2013, 2013.

Bellouin, N., Quaas, J., Gryspeerdt, E., Kinne, S., Stier, P., Watson-Parris, D., Boucher, O., Carslaw, K. S., Christensen, M., Daniau, A.-L., Dufresne, J.-L., Feingold, G., Fiedler, S., Forster, P., Gettelman, A., Haywood, J. M., Lohmann, U., Malavelle, F., Mauritsen, T., McCoy, D. T., Myhre, G., Mülmenstädt, J., Neubauer, D., Possner, A., Rugenstein, M., Sato, Y., Schulz, M., Schwartz, S. E., Sourdeval, O., Storelvmo, T., Toll, V., Winker, D., and Stevens, B.: Bounding Global Aerosol Radiative Forcing of Climate Change, Reviews of Geophysics, 58, e2019RG000660, https://doi.org/10.1029/2019RG000660, 2020.

Bezantakos, S., Varnava, C. K., Papaconstantinou, R., and Biskos, G.: Performance of the Naneos partector 2 multi-metric nanoparticle detector at reduced temperature and pressure conditions, Aerosol Science and Technology, 58, 584–593, https://doi.org/10.1080/02786826.2024.2330471, 2024.

de Boer, G., Calmer, R., Jozef, G., Cassano, J. J., Hamilton, J., Lawrence, D., Borenstein, S., Doddi, A., Cox, C., Schmale, J., Preußer, A., and Argrow, B.: Observing the Central Arctic Atmosphere and Surface with University of Colorado uncrewed aircraft systems, Sci Data, 9, 439, https://doi.org/10.1038/s41597-022-01526-9, 2022.

https://doi.org/10.5194/essd-2026-146
Preprint. Discussion started: 12 March 2026

Brock, C. A., Williamson, C., Kupc, A., Froyd, K. D., Erdesz, F., Wagner, N., Richardson, M., Schwarz, J. P., Gao, R.-S., Katich, J. M., Campuzano-Jost, P., Nault, B. A., Schroder, J. C., Jimenez, J. L., Weinzierl, B., Dollner, M., Bui, T., and Murphy, D. M.: Aerosol size distributions during the Atmospheric Tomography Mission (ATom): methods, uncertainties, and data products, Atmospheric Measurement Techniques, 12, 3081–3099, https://doi.org/10.5194/amt-12-3081-2019, 2019.

Brus, D., Le, V., Kuula, J., and Doulgeris, K.: Data collected by a drone backpack for air quality and atmospheric state measurements during Pallas Cloud Experiment 2022 (PaCE2022), Earth System Science Data Discussions, 1–14, https://doi.org/10.5194/essd-2025-61, 2025.

Calmer, R., Favre, L., Pohorsky, R., Alden, J., and Schmale, J.: Aerosol and meteorological data from a tethered balloon during the CLAVIER campaign Mar-May 2024 at Villum Research Station, Greenland (0), https://doi.org/upcoming, 2026.

Carslaw, K., Lee, L., Reddington, C., Pringle, K., Rap, A., Forster, P., Mann, G., Spracklen, D., Woodhouse, M., and Regayre, L.: Large contribution of natural aerosols to uncertainty in indirect forcing, Nature, 503, 67–71, https://doi.org/10.1038/nature12674, 2013.

Clarke, A. and Kapustin, V.: Hemispheric Aerosol Vertical Profiles: Anthropogenic Impacts on Optical Depth and Cloud Nuclei, Science, 329, 1488–1492, https://doi.org/10.1126/science.1188838, 2010.

Collaud Coen, M., Weingartner, E., Furger, M., Nyeki, S., Prévôt, A. S. H., Steinbacher, M., and Baltensperger, U.: Aerosol climatology and planetary boundary influence at the Jungfraujoch analyzed by synoptic weather types, Atmospheric Chemistry and Physics, 11, 5931–5944, https://doi.org/10.5194/acp-11-5931-2011, 2011.

Creamean, J. M., de Boer, G., Telg, H., Mei, F., Dexheimer, D., Shupe, M. D., Solomon, A., and McComiskey, A.: Assessing the vertical structure of Arctic aerosols using balloon-borne measurements, Atmos. Chem. Phys., 21, 1737–1757, https://doi.org/10.5194/acp-21-1737-2021, 2021.

Engelmann, R., Ansmann, A., Ohneiser, K., Griesche, H., Radenz, M., Hofer, J., Althausen, D., Dahlke, S., Maturilli, M., Veselovskii, I., Jimenez, C., Wiesen, R., Baars, H., Bühl, J., Gebauer, H., Haarig, M., Seifert, P., Wandinger, U., and Macke, A.: Wildfire smoke, Arctic haze, and aerosol effects on mixed-phase and cirrus clouds over the North Pole region during MOSAiC: an introduction, Atmospheric Chemistry and Physics, 21, 13397–13423, https://doi.org/10.5194/acp-21-13397-2021, 2021.

Ferrero, L., Cappelletti, D., Busetto, M., Mazzola, M., Lupi, A., Lanconelli, C., Becagli, S., Traversi, R., Caiazzo, L., Giardi, F., Moroni, B., Crocchianti, S., Fierz, M., Močnik, G., Sangiorgi, G., Perrone, M. G., Maturilli, M., Vitale, V., Udisti, R., and Bolzacchini, E.: Vertical profiles of aerosol and black carbon in the Arctic: a seasonal phenomenology along 2 years (2011–2012) of field campaigns, Atmos. Chem. Phys., 16, 12601–12629, https://doi.org/10.5194/acp-16-12601-2016, 2016.

Fierz, M., Meier, D., Steigmeier, P., and Burtscher, H.: Aerosol Measurement by Induced Currents, Aerosol Science and Technology, 48, 350–357, https://doi.org/10.1080/02786826.2013.875981, 2014.

Fierz, M., Meier, D., Steigmeier, P., and Burtscher, H.: Miniature nanoparticle sensors for exposure measurement and TEM sampling, J. Phys.: Conf. Ser., 617, 012034, https://doi.org/10.1088/1742-6596/617/1/012034, 2015.

Flanner, M. G.: Arctic climate sensitivity to local black carbon, Journal of Geophysical Research: Atmospheres, 118, 1840–1851, https://doi.org/10.1002/jgrd.50176, 2013.

Gast, B., Jimenez, C., Ansmann, A., Haarig, M., Engelmann, R., Fritzsch, F., Floutsi, A. A., Griesche, H., Ohneiser, K., Hofer, J., Radenz, M., Baars, H., Seifert, P., and Wandinger, U.: Invisible aerosol layers: improved lidar detection capabilities by

means of laser-induced aerosol fluorescence, Atmospheric Chemistry and Physics, 25, 3995–4011, https://doi.org/10.5194/acp-25-3995-2025, 2025.

Gordon, H., Glassmeier, F., and T. McCoy, D.: An Overview of Aerosol-Cloud Interactions, in: Clouds and Their Climatic Impacts, American Geophysical Union (AGU), 13–45, https://doi.org/10.1002/9781119700357.ch2, 2023.

Jozef, G. C., Klingel, R., Cassano, J. J., Maronga, B., de Boer, G., Dahlke, S., and Cox, C. J.: Derivation and compilation of lower-atmospheric properties relating to temperature, wind, stability, moisture, and surface radiation budget over the central Arctic sea ice during MOSAiC, Earth System Science Data, 15, 4983–4995, https://doi.org/10.5194/essd-15-4983-2023, 2023.

Kahl, J. D.: Characteristics of the low-level temperature inversion along the Alaskan Arctic coast, International Journal of Climatology, 10, 537–548, https://doi.org/10.1002/joc.3370100509, 1990.

Kanji, Z. A., Ladino, L. A., Wex, H., Boose, Y., Burkert-Kohn, M., Cziczo, D. J., and Krämer, M.: Overview of Ice Nucleating Particles, Meteorological Monographs, 58, 1.1-1.33, https://doi.org/10.1175/amsmonographs-d-16-0006.1, 2017.

Lappin, F., de Boer, G., Klein, P., Hamilton, J., Spencer, M., Calmer, R., Segales, A. R., Rhodes, M., Bell, T. M., Buchli, J., Britt, K., Asher, E., Medina, I., Butterworth, B., Otterstatter, L., Ritsch, M., Puxley, B., Miller, A., Jordan, A., Gomez-Faulk, C., Smith, E., Borenstein, S., Thornberry, T., Argrow, B., and Pillar-Little, E.: Data collected using small uncrewed aircraft systems during the TRacking Aerosol Convection interactions ExpeRiment (TRACER), Earth System Science Data, 16, 2525–2541, https://doi.org/10.5194/essd-16-2525-2024, 2024.

Lei, L., Sun, Y., Ouyang, B., Qiu, Y., Xie, C., Tang, G., Zhou, W., He, Y., Wang, Q., Cheng, X., Fu, P., and Wang, Z.: Vertical Distributions of Primary and Secondary Aerosols in Urban Boundary Layer: Insights into Sources, Chemistry, and Interaction with Meteorology, Environ. Sci. Technol., 55, 4542–4552, https://doi.org/10.1021/acs.est.1c00479, 2021.

Lenschow, D. and Spyers-Duran, P.: Measurement Techniques: Air motion sensing, National Center for Atmospheric Research, 1989.

Liu, X., Hadiatullah, H., Zhang, X., Hill, L. D., White, A. H. A., Schnelle-Kreis, J., Bendl, J., Jakobi, G., Schloter-Hai, B., and Zimmermann, R.: Analysis of mobile monitoring data from the microAeth® MA200 for measuring changes in black carbon on the roadside in Augsburg, Atmos. Meas. Tech., 14, 5139–5151, https://doi.org/10.5194/amt-14-5139-2021, 2021a.

Liu, Z., Osborne, M., Anderson, K., Shutler, J. D., Wilson, A., Langridge, J., Yim, S. H. L., Coe, H., Babu, S., Satheesh, S. K., Zuidema, P., Huang, T., Cheng, J. C. H., and Haywood, J.: Characterizing the performance of a POPS miniaturized optical particle counter when operated on a quadcopter drone, Atmos. Meas. Tech., 14, 6101–6118, https://doi.org/10.5194/amt-14-6101-2021, 2021b.

Lonardi, M., Hirschy, M. L., Calmer, R., Favre, L., Pohorsky, R., Alden, J., and Schmale, J.: Aerosol and meteorological data from the EERL Helikite operated between September 2022 and October 2022 during the Pallas Cloud Experiment 2022, https://doi.org/10.5281/zenodo.18663940, 2026.

Ogren, J. A.: Comment on "Calibration and Intercomparison of Filter-Based Measurements of Visible Light Absorption by Aerosols," null, 44, 589–591, https://doi.org/10.1080/02786826.2010.482111, 2010.

The 2022 GCOS Implementation Plan (GCOS-244): https://library.wmo.int/records/item/58104-the-2022-gcos-implementation-plan-gcos-244, last access: 14 July 2025.

https://doi.org/10.5194/essd-2026-146
Preprint. Discussion started: 12 March 2026

Pace, G., Junkermann, W., Vitali, L., Di Sarra, A., Meloni, D., Cacciani, M., Cremona, G., Iannarelli, A. M., and Zanini, G.: On the complexity of the boundary layer structure and aerosol vertical distribution in the coastal Mediterranean regions: a case study, Tellus B: Chemical and Physical Meteorology, 67, 27721, https://doi.org/10.3402/tellusb.v67.27721, 2015.

Pasquier, J., Henneberger, J., Wieder, J., David, R., Li, G., Carlsen, T., Gierens, R., Ebell, K., Maturilli, M., Ritter, C., Neuber, R., Zieger, P., and Lohmann, U.: Understanding Microphysical Processes in Arctic Mixed-Phase Clouds from Balloon-Borne Holographic Instrument, https://ui.adsabs.harvard.edu/abs/2020AGUFMA011.0007P, 2020.

Patel, A. K. and Divecha, J.: Modified exponentially weighted moving average (EWMA) control chart for an analytical process data, 2, 12–20, 2010.

Pätzold, F., Bretschneider, L., Nowak, S., Brandt, B., Schlerf, A., Asmussen, M. O., Bollmann, S., Bärfuss, K., Harm-Altstädter, B., Hecker, P., Wehner, B., van der Wall, B. G., Sachs, T., Huntrieser, H., Roiger, A., and Lampert, A.: HELiPOD—Revolution and evolution of a helicopter-borne measurement system for multidisciplinary research in demanding environments, Elementa: Science of the Anthropocene, 11, 00031, https://doi.org/10.1525/elementa.2023.00031, 2023.

Pilz, C., Düsing, S., Wehner, B., Müller, T., Siebert, H., Voigtländer, J., and Lonardi, M.: CAMP: an instrumented platform for balloon-borne aerosol particle studies in the lower atmosphere, Atmos. Meas. Tech., 15, 6889–6905, https://doi.org/10.5194/amt-15-6889-2022, 2022.

Pilz, C., Lonardi, M., Egerer, U., Siebert, H., Ehrlich, A., Heymsfield, A. J., Schmitt, C. G., Shupe, M. D., Wehner, B., and Wendisch, M.: Profile observations of the Arctic atmospheric boundary layer with the BELUGA tethered balloon during MOSAiC, Sci Data, 10, 534, https://doi.org/10.1038/s41597-023-02423-5, 2023.

Pilz, C., Cassano, J. J., de Boer, G., Kirbus, B., Lonardi, M., Pöhlker, M., Shupe, M. D., Siebert, H., Wendisch, M., and Wehner, B.: Tethered balloon measurements reveal enhanced aerosol occurrence aloft interacting with Arctic low-level clouds, Elementa: Science of the Anthropocene, 12, 00120, https://doi.org/10.1525/elementa.2023.00120, 2024.

Pohorsky, R., Baccarini, A., Tolu, J., Winkel, L. H. E., and Schmale, J.: Modular Multiplatform Compatible Air Measurement System (MoMuCAMS): a new modular platform for boundary layer aerosol and trace gas vertical measurements in extreme environments, Atmospheric Measurement Techniques, 17, 731–754, https://doi.org/10.5194/amt-17-731-2024, 2024.

Pohorsky, R., Schmale, J., and Bacarini, A.: Aerosol, trace gas and meteorological data measured at the University of Alaska Fairbanks Farm site in Fairbanks, Alaska during the Alaskan Layered Pollution And Chemical Analysis (ALPACA)-2022 field study, https://doi.org/10.18739/A2CR5NF36, 2025a.

Pohorsky, R., Baccarini, A., Brett, N., Barret, B., Bekki, S., Pappaccogli, G., Dieudonné, E., Temime-Roussel, B., D'Anna, B., Cesler-Maloney, M., Donateo, A., Decesari, S., Law, K. S., Simpson, W. R., Fochesatto, J., Arnold, S. R., and Schmale, J.: In situ vertical observations of the layered structure of air pollution in a continental high-latitude urban boundary layer during winter, Atmospheric Chemistry and Physics, 25, 3687–3715, https://doi.org/10.5194/acp-25-3687-2025, 2025b.

Pohorsky, Roman, Calmer, Radiance, Brooks, Ian, Guy, Heather, Fauré, Nicolas, Haberstock, Lea, Creamean, Jessie, Mavis, Camille, and Schmale, Julia: Vertical in situ measurements of aerosols and meteorological variables from expedition ARTofMELT, Arctic Ocean, 2023 (1), https://doi.org/10.17043/ODEN-ARTOFMELT-2023-AEROSOLS-VERTICAL-1, 2025.

Porter, G. C. E., Sikora, S. N. F., Adams, M. P., Proske, U., Harrison, A. D., Tarn, M. D., Brooks, I. M., and Murray, B. J.: Resolving the size of ice-nucleating particles with a balloon deployable aerosol sampler: the SHARK, Atmos. Meas. Tech., 13, 2905–2921, https://doi.org/10.5194/amt-13-2905-2020, 2020.

https://doi.org/10.5194/essd-2026-146
Preprint. Discussion started: 12 March 2026

Prasad, P., Basha, G., and Ratnam, M. V.: Is the atmospheric boundary layer altitude or the strong thermal inversions that control the vertical extent of aerosols?, Science of The Total Environment, 802, 149758, https://doi.org/10.1016/j.scitotenv.2021.149758, 2022.

Radenz, M., Engelmann, R., Henning, S., Schmithüsen, H., Baars, H., Frey, M. M., Weller, R., Bühl, J., Jimenez, C., Roschke, J., Muser, L. O., Wullenweber, N., Zeppenfeld, S., Griesche, H., Wandinger, U., and Seifert, P.: Ground-Based Remote Sensing of Aerosol, Clouds, Dynamics, and Precipitation in Antarctica: First Results from the 1-Year COALA Campaign at Neumayer Station III in 2023, Bulletin of the American Meteorological Society, 105, E1438–E1457, https://doi.org/10.1175/BAMS-D-22-0285.1, 2024.

Renard, J.-B., Dulac, F., Berthet, G., Lurton, T., Vignelles, D., Jégou, F., Tonnelier, T., Jeannot, M., Couté, B., Akiki, R., Verdier, N., Mallet, M., Gensdarmes, F., Charpentier, P., Mesmin, S., Duverger, V., Dupont, J.-C., Elias, T., Crenn, V., Sciare, J., Zieger, P., Salter, M., Roberts, T., Giacomoni, J., Gobbi, M., Hamonou, E., Olafsson, H., Dagsson-Waldhauserova, P., Camy-Peyret, C., Mazel, C., Décamps, T., Piringer, M., Surcin, J., and Daugeron, D.: LOAC: a small aerosol optical counter/sizer for ground-based and balloon measurements of the size distribution and nature of atmospheric particles – Part 2: First results from balloon and unmanned aerial vehicle flights, Atmospheric Measurement Techniques, 9, 3673–3686, https://doi.org/10.5194/amt-9-3673-2016, 2016.

Rosati, B., Gysel, M., Rubach, F., Mentel, T. F., Goger, B., Poulain, L., Schlag, P., Miettinen, P., Pajunoja, A., Virtanen, A., Bialek, J., Klein Baltink, H., Henzing, J. S., Größ, J., Gobbi, G. P., Wiedensohler, A., Kiendler-Scharr, A., O'Dowd, C., Decesari, S., Facchini, M. C., Weingartner, E., and Baltensperger, U.: Vertical profiling of aerosol hygroscopic properties in the planetary boundary layer during the PEGASOS campaigns, Atmos. Chem. Phys. Discuss., 15, 9445–9505, https://doi.org/10.5194/acpd-15-9445-2015, 2015.

Rosenfeld, D., Andreae, M. O., Asmi, A., Chin, M., de Leeuw, G., Donovan, D. P., Kahn, R., Kinne, S., Kivekäs, N., Kulmala, M., Lau, W., Schmidt, S., Suni, T., Wagner, T., Wild, M., and Quaas, J.: Global observations of aerosol-cloud-precipitation-climate interactions, Reviews of Geophysics, https://doi.org/10.1002/2013RG000441, 2014.

Rotach, M. W. and Zardi, D.: On the boundary-layer structure over highly complex terrain: Key findings from MAP, Quarterly Journal of the Royal Meteorological Society, 133, 937–948, https://doi.org/10.1002/qj.71, 2007.

Samset, B. H., Myhre, G., Schulz, M., Balkanski, Y., Bauer, S., Berntsen, T. K., Bian, H., Bellouin, N., Diehl, T., Easter, R. C., Ghan, S. J., Iversen, T., Kinne, S., Kirkevåg, A., Lamarque, J.-F., Lin, G., Liu, X., Penner, J. E., Seland, Ø., Skeie, R. B., Stier, P., Takemura, T., Tsigaridis, K., and Zhang, K.: Black carbon vertical profiles strongly affect its radiative forcing uncertainty, Atmos. Chem. Phys., 13, 2423–2434, https://doi.org/10.5194/acp-13-2423-2013, 2013.

Schlosser, J. S., Stamnes, S., Burton, S. P., Cairns, B., Crosbie, E., Van Diedenhoven, B., Diskin, G., Dmitrovic, S., Ferrare, R., Hair, J. W., Hostetler, C. A., Hu, Y., Liu, X., Moore, R. H., Shingler, T., Shook, M. A., Thornhill, K. L., Winstead, E., Ziemba, L., and Sorooshian, A.: Polarimeter + Lidar–Derived Aerosol Particle Number Concentration, Front. Remote Sens., 3, https://doi.org/10.3389/frsen.2022.885332, 2022.

Schmale, J., Zieger, P., and Ekman, A. M. L.: Aerosols in current and future Arctic climate, Nature Climate Change, https://doi.org/10.1038/s41558-020-00969-5, 2021.

Schmale, J., Pohorsky, R., and Baccarini, A.: Aerosol and meteorological data from a tethered balloon during the Brigerbad campaign September-October 2021 (Switzerland), https://doi.org/10.5281/zenodo.18327462, 2026.

Shupe, M. D. and Intrieri, J. M.: Cloud Radiative Forcing of the Arctic Surface: The Influence of Cloud Properties, Surface Albedo, and Solar Zenith Angle, Journal of Climate, 17, 616–628, https://doi.org/10.1175/1520-0442(2004)017%253C0616:crfota%253E2.0.co;2, 2004.

https://doi.org/10.5194/essd-2026-146
Preprint. Discussion started: 12 March 2026

Siebert, H., Szodry, K.-E., Egerer, U., Wehner, B., Henning, S., Chevalier, K., Lückerath, J., Welz, O., Weinhold, K., Lauermann, F., Gottschalk, M., Ehrlich, A., Wendisch, M., Fialho, P., Roberts, G., Allwayin, N., Schum, S., Shaw, R. A., Mazzoleni, C., Mazzoleni, L., Nowak, J. L., Malinowski, S. P., Karpinska, K., Kumala, W., Czyzewska, D., Luke, E. P., Kollias, P., Wood, R., and Mellado, J. P.: Observations of Aerosol, Cloud, Turbulence, and Radiation Properties at the Top of the Marine Boundary Layer over the Eastern North Atlantic Ocean: The ACORES Campaign, Bulletin of the American Meteorological Society, 102, E123–E147, https://doi.org/10.1175/BAMS-D-19-0191.1, 2021.

Simpson, W. R., Mao, J., Fochesatto, G. J., Law, K. S., DeCarlo, P. F., Schmale, J., Pratt, K. A., Arnold, S. R., Stutz, J., Dibb, J. E., Creamean, J. M., Weber, R. J., Williams, B. J., Alexander, B., Hu, L., Yokelson, R. J., Shiraiwa, M., Decesari, S., Anastasio, C., D'Anna, B., Gilliam, R. C., Nenes, A., St. Clair, J. M., Trost, B., Flynn, J. H., Savarino, J., Conner, L. D., Kettle, N., Heeringa, K. M., Albertin, S., Baccarini, A., Barret, B., Battaglia, M. A., Bekki, S., Brado, T. J., Brett, N., Brus, D., Campbell, J. R., Cesler-Maloney, M., Cooperdock, S., Cysneiros de Carvalho, K., Delbarre, H., DeMott, P. J., Dennehy, C. J. S., Dieudonné, E., Dingilian, K. K., Donateo, A., Doulgeris, K. M., Edwards, K. C., Fahey, K., Fang, T., Guo, F., Heinlein, L. M. D., Holen, A. L., Huff, D., Ijaz, A., Johnson, S., Kapur, S., Ketcherside, D. T., Levin, E., Lill, E., Moon, A. R., Onishi, T., Pappaccogli, G., Perkins, R., Pohorsky, R., Raut, J.-C., Ravetta, F., Roberts, T., Robinson, E. S., Scoto, F., Selimovic, V., Sunday, M. O., Temime-Roussel, B., Tian, X., Wu, J., and Yang, Y.: Overview of the Alaskan Layered Pollution and Chemical Analysis (ALPACA) Field Experiment, ACS EST Air, https://doi.org/10.1021/acsestair.3c00076, 2024.

Solidakis, O.: Improvement and testing of a cloud droplet analyzer for balloon-borne applications, Intership Report, EPFL, 2024.

Temel, Y., Calmer, R., Alden, J., Lonardi, M., Surdu, M., Favre, L., Pohorsky, R., and Schmale, J.: Aerosol and meteorological data from a the EERL Helikite in February 2024 in Turtmann, Switzerland, https://doi.org/10.5281/zenodo.18327709, 2026a.

Temel, Y., Londardi, M., and Schmale, J.: Aerosol and meteorological data from the EERL helikites during the ORACLES field campaign between December 2024 and February 2025 at Neumayer Station III, Antarctica, https://doi.org/10.5281/zenodo.18664026, 2026b.

Thomas, M. A., Devasthale, A., Tjernström, M., and Ekman, A. M. L.: The Relation Between Aerosol Vertical Distribution and Temperature Inversions in the Arctic in Winter and Spring, Geophysical Research Letters, 46, 2836–2845, https://doi.org/10.1029/2018gl081624, 2019.

Wiedensohler, A., Birmili, W., Nowak, A., Sonntag, A., Weinhold, K., Merkel, M., Wehner, B., Tuch, T., Pfeifer, S., Fiebig, M., Fjäraa, A. M., Asmi, E., Sellegri, K., Depuy, R., Venzac, H., Villani, P., Laj, P., Aalto, P., Ogren, J. A., Swietlicki, E., Williams, P., Roldin, P., Quincey, P., Hüglin, C., Fierz-Schmidhauser, R., Gysel, M., Weingartner, E., Riccobono, F., Santos, S., Grüning, C., Faloon, K., Beddows, D., Harrison, R., Monahan, C., Jennings, S. G., O'Dowd, C. D., Marinoni, A., Horn, H. G., Keck, L., Jiang, J., Scheckman, J., McMurry, P. H., Deng, Z., Zhao, C. S., Moerman, M., Henzing, B., de Leeuw, G., Löschau, G., and Bastian, S.: Mobility particle size spectrometers: harmonization of technical standards and data structure to facilitate high quality long-term observations of atmospheric particle number size distributions, Atmos. Meas. Tech., 5, 657–685, https://doi.org/10.5194/amt-5-657-2012, 2012.

WMO: Guide to Instruments and Methods of Observation, WMO, Geneva, Switzerland, https://library.wmo.int/records/item/68695-guide-to-instruments-and-methods-of-observation, 2025.

Zelinka, M. D., Andrews, T., Forster, P. M., and Taylor, K. E.: Quantifying components of aerosol-cloud-radiation interactions in climate models, Journal of Geophysical Research: Atmospheres, 119, 7599–7615, https://doi.org/10.1002/2014JD021710, 2014.